

## MASTER

### Temperature measurements on steam injection in a cross-flow and a non-isothermal diffuse-interface model for two-phase flows

van Deurzen, L.G.M.

*Award date:*  
2010

[Link to publication](#)

#### **Disclaimer**

This document contains a student thesis (bachelor's or master's), as authored by a student at Eindhoven University of Technology. Student theses are made available in the TU/e repository upon obtaining the required degree. The grade received is not published on the document as presented in the repository. The required complexity or quality of research of student theses may vary by program, and the required minimum study period may vary in duration.

#### **General rights**

Copyright and moral rights for the publications made accessible in the public portal are retained by the authors and/or other copyright owners and it is a condition of accessing publications that users recognise and abide by the legal requirements associated with these rights.

- Users may download and print one copy of any publication from the public portal for the purpose of private study or research.
- You may not further distribute the material or use it for any profit-making activity or commercial gain

**Temperature measurements on steam injection in a cross-flow and a non-isothermal diffuse-interface model for two-phase flows**

L.G.M.van Deurzen

Reportnumber: WCP201006  
Supervisors: dr. J.G.M. Kuerten  
dr. C.W.M. van der Geld  
ir. N. Clerx  
ir. A. Pecenko  
Professor: prof.dr.ir. J.J.H. Brouwers

Eindhoven University of Technology  
Department of Mechanical Engineering  
Process Technology

Eindhoven, July 2010

# Abstract

Steam injection is used in industrial applications like fast heating. To be able to understand the principles of steam injection better, temperature measurements are performed during steam injection in a cross-flow of water, and  $\Delta T$  is determined as the temperature difference with the cross-flow. In the measurements, steam condenses close to the injector. The remaining part of the flow field can be described as a single phase jet in cross-flow. Maximum  $\Delta T$  trajectories for the jet compare well to the trajectories that are found in literature.

An interesting feature of the temperature-difference fields is the occurrence of a plume of high  $\Delta T$  that is advected with the cross-flow on the side of the injector. This plume is observed for high cross-flow temperatures while for low cross-flow temperatures it can not be seen. An explanation for the plume could be found in the way the steam condenses. For a higher cross-flow temperature the steam pockets penetrate further in the cross-flow as observed by Clerx [6].

To predict the flow fields for steam injection a model should be developed that is able to describe two-phase flow including phase change. An isothermal diffuse interface method for two-phase flows with a Van der Waals equation of state is extended with an energy equation to incorporate the effects of heat transfer and the energy from phase change. The method works well and is able to predict flows for two dimensional test cases. For drop retraction and evaporation the model describes the flow as expected. Drop collision simulations are dependent on the velocity of the drops but also on the heat transfer coefficient. For a low heat transfer coefficient the resistance for coalescence is high and drops have been found to bounce back for low collision velocities. For higher heat transfer coefficient, coalescence occurs as expected.

The length scale for which the diffuse interface method can be applied is quite small and the fluid should be close to its critical point. The test cases can however be used to validate methods that are applicable to larger length scales.

# Acknowledgements

This Report would not have been possible without the help of many people.

For his advice and extensive guidance on the numerical part I'd like to thank Hans Kuerten. Advancements on our diffuse-interface method as presented here would also not have been possible without previous efforts from Alessandro Pecenko on this method.

I'd like to thank Nicole Clerx for her help with the measurements and the analysis of these. Her work on the steam injection setup in the previous years made it possible to perform the measurements fast and efficient. I'd like to thank Cees van der Geld for his comments and advice on the interpretation of the data that was obtained from the temperature measurements

For keeping the morale high during the many hours I spend behind my desk, special thanks go to my fellow students Thiemo Roos and Sander Derks. I would also like to use this opportunity to thank all my friends and my family for supporting me throughout my studies.

# Contents

<b>Abstract</b>	<b>2</b>
<b>Acknowledgements</b>	<b>3</b>
<b>1 Introduction</b>	<b>6</b>
<b>2 Temperature measurements on steam injection in cross-flow</b>	<b>7</b>
2.1 Literature review . . . . .	7
2.2 Experimental method . . . . .	10
2.3 Results . . . . .	13
2.4 Analysis . . . . .	16
2.4.1 Jet temperature center line . . . . .	16
2.4.2 Jet maximum Temperature . . . . .	20
2.4.3 Comparison with velocity fields . . . . .	22
2.4.4 The plume . . . . .	22
<b>3 Nonisothermal simulation of two phase flow with a diffuse interface model</b>	<b>27</b>
3.1 Diffuse interface method . . . . .	27
3.2 The governing equations . . . . .	28
3.2.1 An approximation of the internal energy for a fluid described by a Van der Waals equation of state . . . . .	30
3.3 The Numerical method . . . . .	31
3.4 One-dimensional simulations . . . . .	32
3.5 Two-dimensional simulations . . . . .	35
3.5.1 Drop retraction . . . . .	36
3.5.2 Drop evaporation . . . . .	40
3.5.3 Drop collision . . . . .	42
<b>4 Conclusions</b>	<b>51</b>
<b>A Influence of the temperature sensors on the mean flow</b>	<b>55</b>
<b>B Calibration of Pt-100 temperature sensors</b>	<b>59</b>
<b>C Experiments and settings for temperature measurements on steam injection</b>	<b>61</b>
<b>D Thin plate spline interpolation with Matlab</b>	<b>64</b>

<b>E</b>	<b>Description of the simulations</b>	<b>66</b>
E.1	One dimensional simulations . . . . .	66
E.2	Drop retraction simulations . . . . .	67
E.3	Drop evaporation . . . . .	69
E.4	Drop collision . . . . .	70
<b>F</b>	<b>Two-dimensional model for the governing equations</b>	<b>73</b>
<b>G</b>	<b>Derivation of conservative form of the energy equation</b>	<b>75</b>
<b>H</b>	<b>Numerical validation of 1D stability analysis</b>	<b>76</b>
<b>I</b>	<b>Programming</b>	<b>79</b>
I.1	Experimental . . . . .	79
I.2	Numerical . . . . .	80
<b>J</b>	<b>Saturation properties and surface tension</b>	<b>83</b>
J.1	Saturation properties . . . . .	83
J.2	Surface tension . . . . .	84

# Chapter 1

## Introduction

Steam injection is often used in industrial applications. Large amounts of heat can be transferred to a cross-flow by direct steam injection. The amount of heat that is supplied by a steam flow is known. The temperature increase that results from this is therefore not hard to compute. This yields only information on the average temperature increase. Locally the temperature can increase more because the heat from the steam is not distributed evenly over the cross-flow. It is important to obtain knowledge about steam injection when fast mixing is required or when high local temperatures need to be avoided.

In chapter 2 temperature measurements on a steam jet in cross-flow will be described. Together with the investigation of the condensation of the steam in the jet and velocity fields that are obtained for the same test-setup by Clerx [6], this gives a complete overview of the behavior of steam injection in a cross-flow.

In chapter 3, a numerical model for multi-phase flows is developed. The method uses a diffuse interface method with the Van der Waals equation as state-equation. Although it can only be used for a limited set of cases, it will describe the behavior of a Van der Waals fluid quite accurately. Assuming that the Van der Waals equation gives a good approximation for the state of the fluid, the model can be used to validate future models.

## Chapter 2

# Temperature measurements on steam injection in cross-flow

Heating is one of the major applications of steam injection in industry. For these applications, a common requirement is that the temperature rises uniformly. Some applications may require that the temperature in the cross-flow does not rise too much locally. To be able to fulfill such requirements. It is necessary to obtain general knowledge on steam injection that could be applied in future designs of industrial steam injectors. In earlier work by Clerx [6], condensation of steam injected in a cross-flow is visualized and velocity fields are obtained. For this a test setup was used in which steam can be injected in a cross-flow of water. This chapter is concerned with obtaining temperature measurements for the same test setup.

### 2.1 Literature review

In earlier research by Clerx [6] it has been observed that steam condenses quite close to the injection point. At lower steam mass fluxes, oscillatory condensation phenomena occur. Steam pockets grow and disappear in fairly constant cycles. The shape and size of the steam pockets as well as the growth time are observed to be dependent on the steam mass flux,  $G$ , cross-flow temperature,  $T_{cf}$ , and the cross-flow rate  $Q_{cf}$ . The penetration depth of the steam pockets in the cross flow is observed to be of the order of the injector diameter. The penetration depth is here defined as the maximum distance the steam travels till it condenses.

A higher  $T_{cf}$  increases both the penetration depth and the cycle time. This can be explained by a lower heat transfer rate from the steam pocket to the liquid due to a smaller temperature difference.

$G$  influences the structure of the vapor-liquid interface. For higher  $G$ , the interface shows more wrinkling. This, according to Clerx [6], implies higher shear and heat transfer rates due to the higher relative velocity. The growth time of the pockets becomes smaller for higher mass flux. The penetration depth is hardly influenced for high  $T_{cf}$  (65 °C) while for low  $T_{cf}$  (25 °C) the penetration depth is observed to increase slightly for lower values of  $G$ .

The steam pocket shapes that have been observed just before detachment are summarized by Clerx [6] for different  $T_{cf}$  and  $G$  in figure 2.1. Compared to steam injection without cross-flow, the penetration depth is smaller for a flow with cross-flow.

Further from the injector the steam is condensed and there is a single phase flow. The flow field in this region shows a jet structure. figure 2.2 shows schematically the test setup



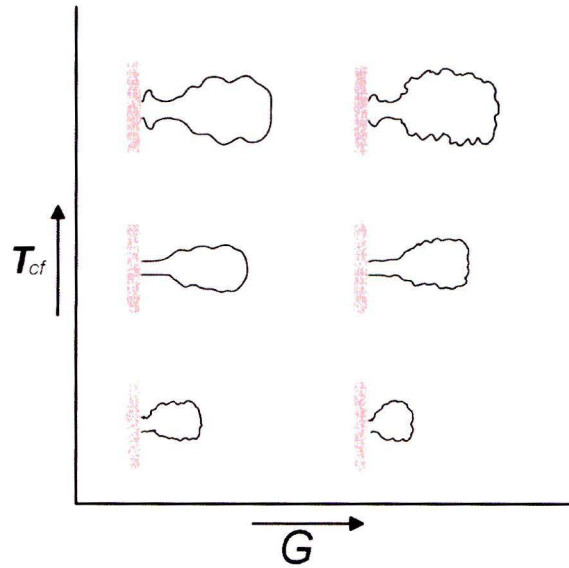


Figure 2.1: Impact of steam mass flux,  $G$ , and cross flow temperature,  $T_{cf}$ , maximum steam pocket shapes at detachment as observed by Clerx [6]

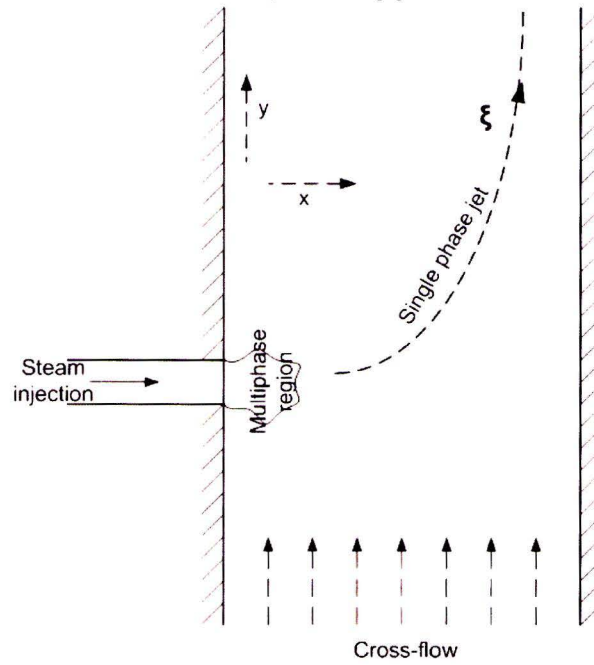


Figure 2.2: Overview of the steam injection in a cross-flow as observed in the test setup

as used by Clerx with the region of two-phase-flow near the injection point and the region of the single-phase jet further from the injection point of the steam. The flow in later region is compared with literature on turbulent jets in cross flow. The jets that are found in literature are created by injecting a fluid of the same phase in a cross flow. The velocity ratio,  $r$ , is used to characterize jets in cross flow. The velocity ratio is defined as the square root of the momentum ratio  $J$ :

$$r = J^{1/2} = \left( \frac{\rho_j U_j^2}{\rho_{cf} U_{cf}^2} \right)^{1/2} \quad (2.1)$$

Here  $\rho$  is the mass density and  $U$  is the velocity where the subscript  $j$  refers to the jet and the subscript  $cf$  refers to the cross-flow. In our report, the bulk velocities are used to calculate the momentum ratios.

To be able to understand the results from our measurements and it is necessary that we describe the structure of single phase jets in cross-flows in more detail. Smith and Mungal [16] describe three distinct regions for jets in cross flow. Close to the entrance, there is the vortex interaction region. In this region the cross flow, flows around the jet column. A little further downstream, the jet develops a counter-rotating vortex pair (CVP). The region in which the CVP is developing is called the near field while the region in which the CVP is developed is called the far field. Three length scales are used to characterize the jets. There is the exit diameter  $d$  which is a characteristic length scale for the Vortex interaction region. The length scale  $rd$  is used to scale the trajectories and the dimensions of the jet.

Smith and Mungal [16] show that the concentration center lines scale with length scale  $rd$ . The concentration centerline is defined as the locus of the points with maximum concentration. Assuming that the Peclet numbers for thermal and mass diffusion are large, which is a good assumption for a turbulent flow, the temperature and concentration center lines will look the same as they both function as a passive tracer. The Peclet number for thermal diffusion is defined by:  $Pe_T = \frac{LU}{\alpha}$  and the one for mass diffusion  $Pe_m = \frac{LU}{D}$ . Here  $L$  and  $U$  are a characteristic length scale and a characteristic velocity.  $\alpha$  is the heat diffusivity and  $D$  is the mass diffusion coefficient. Kamotani and Greber (1972) [9] find that the velocity center line penetrates further in the cross-flow than the temperature center line.

Smith and Mungal [16] inject from a nozzle in a wall. Kamotani and Greber (1972) [9] observed that the inlet conditions are important. The trajectories changed about 12 % when the injection was done with a pipe intruding the cross-flow. Pratte and Baines [14] are able to collapse the centerline profiles with the correlation:

$$\frac{x}{rd} = A \left( \frac{y}{rd} \right)^m \quad (2.2)$$

With  $A=2.05$  and  $m=0.28$ ;  $y$  is the coordinate in the cross-flow direction and  $x$  is the coordinate in the jet direction. In figure 2.2, the directions  $x$  and  $y$  are shown. The origin for these coordinates is the injection point. Smith and Mungal [16] find values of  $A = 1.5$  and  $m=0.27$ . The difference may be explained by the different injection methods.

A coordinate along the jet axis,  $\xi$ , can be defined as the distance traveled along the jet, This is shown schematically in figure 2.2. The origin for this coordinate is injection point. Smith and Mungal find that the transition from the near to the far field takes place at a distance  $\xi = \xi_t$  where the transition distance is found to be:  $\xi_t = 0.3r^2d$ .

The concentration decline is found by Smith and Mungal [16] to be  $\xi^{-1.3}$  in the near field and  $\xi^{-2/3}$  in the far field. In a log-log plot a clear transition between the near and a

far field can be observed. The vortex interaction region shows no decline of concentration. This was already observed by Kamotani and Greber (1972) [9]. They report in this region a development of the flow from a so called 'potential core' with uniform velocity to a Gaussian looking profile with the same maximum velocity.

Kamotani and Greber (1972) [9] performed measurements for jet-Reynolds numbers in a range of  $Re_j = 2800$  to  $Re_j = 4200$ . Smith and Mungal [16] investigated the influence of the Reynolds number on the center line concentration decay, for Reynolds numbers 8400 to 33000. Both papers report that the Reynolds number is of little importance for turbulent jets in cross-flow.

The internal Froude number is a measure for the importance of the buoyancy forces compared to the inertial forces. The internal Froude number is defined in Kunudu [11] as:

$$Fr' \equiv \left[ \frac{\text{Inertiaforce}}{\text{Buoyancyforce}} \right]^{1/2} = \frac{U}{\sqrt{g'l}} \quad (2.3)$$

For  $U$  the cross flow velocity is used and for the length  $l$  the diameter of the injector is used.  $g'$  represents the reduced gravity. The reduced gravity for the hot single phase jet can be calculated by  $g' = g\beta\Delta T$ , with  $\beta$  the cubic expansion coefficient. For our measurements the temperature difference between the jet and the cross flow,  $\Delta T$ , is of the order of 5 ° C. The internal Froude number is for all our cases of the order 10 till 100. This means that the effect of buoyancy can be neglected in the single phase hot jet.

The test setup that is used is confined while present findings on the turbulent jets holds for unconfined jets. Kamotani and Greber (1974) [10] show that confinement of the cross-flow has almost no effect on the flow field for small momentum ratios. For higher momentum ratio, the jet would flow very close to the wall and could even impinge on it. In that case the flow would be affected. But even for the cases where the jets impinge on the wall the flow only changes close to the wall on which the jet impinges.

## 2.2 Experimental method

Temperature measurements are performed in the test setup as described by Clerx [6]. The test setup is filled with demineralized water. The temperature is controlled with a heater and a heat exchanger. An expansion tank, which is connected to pressurized air, is used to set the pressure. An electrically controlled valve that opens when the pressure exceeds the set-point keeps the pressure at 3 bar during the measurements. The measurement section has a square inner cross-section of 30x30 mm<sup>2</sup>. It is optically accessible from three sides. The water flows in upward direction trough the section. Before entering the measurement section, the water flows through a channel with a identical cross-section and a length of 1200 mm (40Dh). This ensures that a developed turbulent flow enters the measurement section. Saturated or slightly superheated steam is injected from the side of the measurement section. The steam is injected trough a circular hole with a 2 mm diameter. The mass flow-rate of the steam is controlled with a combination of a Coriolis mass flow meter and an electrically controlled valve. The supply line of the steam is heated to avoid condensation.

A schematic representation of the test setup is shown in figure 2.3. There are three temperature sensors in the measurement section. The three PT-100 temperature sensors (Class A, diameter 1 mm) are put in the measurement section from the side as shown schematically in figure 2.4 Here the temperature sensors are depicted with their systematic names. The

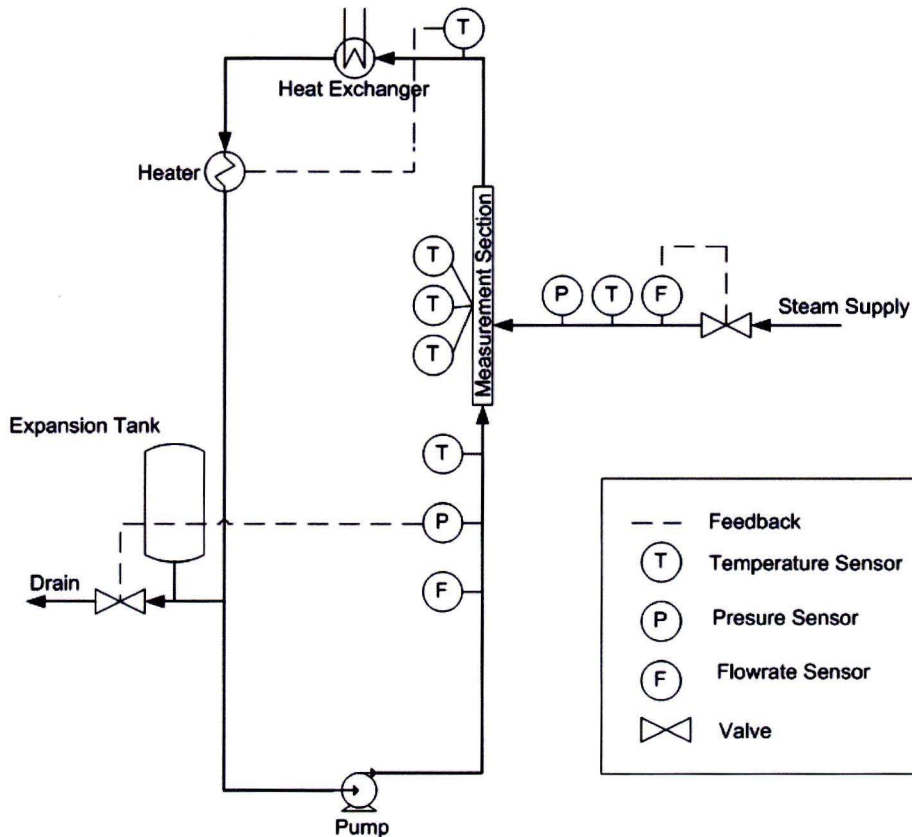


Figure 2.3: Schematic representation of the test setup

temperature sensors can slide through the domain due to the adjustable position of the cylinder on which the sensors are mounted. The sensors slide in a  $40^\circ$  angle to the horizontal. Data of the sensors is logged with a PC during the measurements.

The goal of the temperature measurements is to obtain temperature fields during steam injection. To this end, the temperature in the measurement section is measured with the three PT-100 temperature sensors at 10 positions in the measurement section. At each position the temperature is measured for 2 minutes. Data from the sensors is written to file every second. The transient condensation of the steam pockets has a typical time scale in the order of milliseconds while the response time of the sensors is in the order of seconds. It is therefore impossible to measure instantaneous value of the temperature. The value of the sensors can only be used to obtain results for the mean value of the temperature.

During the measurements, the settings of the test setup are kept as constant as possible. The measured value for the pressure,  $P_l$ , Volume flow of the cross flow,  $Q_l$ , steam mass flow  $\dot{m}$ , and the temperature of the steam,  $T_v$ , deviate not more than 4% from their setpoint. The temperature of the cross flow can be kept constant within a range of  $\pm 0.5^\circ\text{C}$ . Due to this error, absolute temperature fields would be inaccurate. The temperature difference,  $\Delta T$ , defined as the mean difference between the measured temperatures in the measurement section and the temperature of the cross flow over the 2 minute time interval, will be used to obtain more accurate fields. The temperature as measured with the Pt-100 sensor TI-104

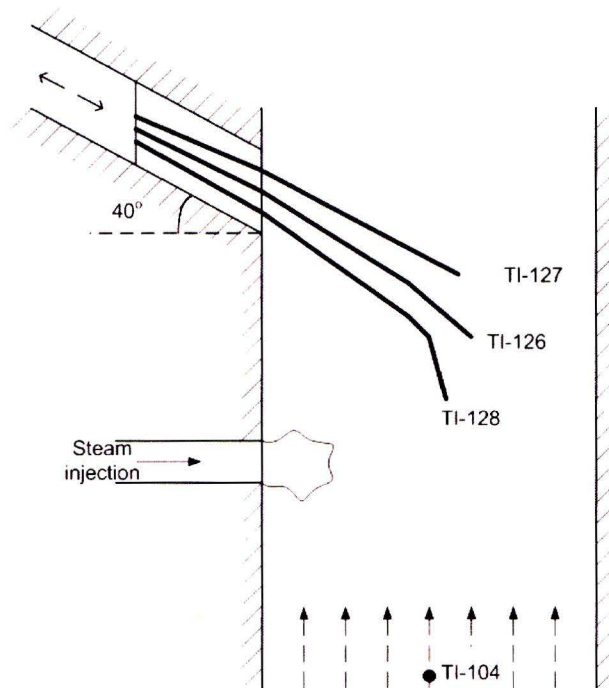


Figure 2.4: Schematic representation of the measurement section

(Class B, diameter 1.5 mm) that is located 2 m upstream is used to determine the temperature of the cross flow.

The temperature sensors can slide by adjusting the position of the cylinder on which they are mounted. The position of the cylinder can not be determined. A camera is used to determine the location of the tips of the temperature sensors for every measurement. Determination of the location of the temperature sensor is done manually from the pictures. The error in this position can have a value up to the radius of the sensor which is 0.5 mm.

The PT-100 temperature sensors TI-126, TI-127, TI-128 and TI-104 are calibrated with a mercury-in-glass thermometer. A linear correction is applied on the PT-100 sensors. The uncertainty in the temperature for these corrected measurements is 0.1 °C. The calibration data is shown in appendix B.

It is important to investigate the influence of the inserted temperature sensors on the flow field. If the flow field would be changed by the sensors this would mean that the measured temperature field does not represent the situation without the temperature sensor. PIV measurements are performed on the measurement section. No steam injection was present during these measurements. The influence of the sensors on the cross flow was investigated by comparing the results with an undisturbed cross-flow. A thorough discussion of the PIV measurements can be found in appendix A. It is shown that, upstream, the sensors have no influence on the cross-flow. Close to the sensors, the measured flow profile gets disturbed. Influence on the flow can be seen downstream of the sensors. The cross-flow recovers, however, quite fast from disturbances. The maximum disturbance in the mean velocity that has been observed downstream of a sensor in appendix A amounts 20%.

As there are no upstream disturbances, the sensor TI-128 will give a good indication of

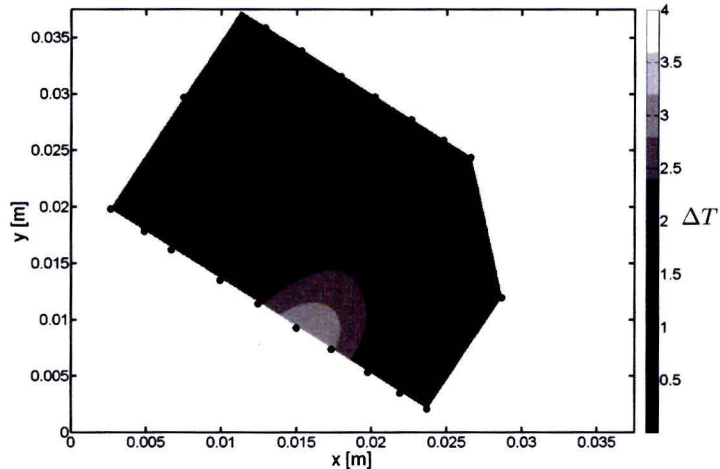


Figure 2.5: Temperature-difference field at 25 ° C for a steam mass flow of 1000 g/h and a cross flow of 0.95 m<sup>3</sup>/h (set 25\_e).  $\Delta T$  in Kelvin.

the temperature. The same holds for TI-126. Because the sensor TI-127 is in the wake of TI-126, the measured temperature by this sensor could deviate from the temperature that would be measured in an undisturbed flow. The cross-flow recovers fast from the disturbance that is introduced by the sensors TI-126 and TI-128. This along with the observation that the sensors are not placed perfectly in one plane makes us conclude that the temperature that the sensor TI-126 measures is still representable for the temperature of an undisturbed flow field. It is therefore chosen to use the data from all sensors in the analysis of the temperature fields. An overview of all sets of measurements and their settings can be found in appendix C.

## 2.3 Results

Several sets of measurements are performed. From the data of a set of measurements, a temperature-difference field can be created in which the temperature difference,  $\Delta T$ , is plotted as function of the coordinates  $x$  and  $y$ . In figure 2.5 one of the temperature-difference fields is shown. The positions of the sensors are depicted by the dots. An interpolation spline is constructed through these points using the Matlab standard function 'tpaps'. This yields a smooth surface through the data points. A more elaborate discussion of the function 'tpaps' can be found in appendix D. In the temperature field in figure 2.5, a jet can be seen. The jet has a higher temperature than the surrounding cross flow. Similar jets are observed for all data sets.

The location of a measurement is the center of the temperature sensor tip. This location is determined manually from a picture of the measurement section during the measurement. The error made in this evaluation amounts up to half the diameter of the sensor. This introduces an expected error in the recorded positions that is:  $\epsilon_{position} = \pm 0.5$  mm.

The measurements for each point is carried out for two minutes at every position. Figure 2.6 shows a typical sensor output for a temperature measurement. The output of the three

sensors in the measurement section; TI-126, TI-127, T-128 and the sensor upstream in the cross-flow; TI-104 is shown. The temperature is measured every second. We now define the instantaneous temperature difference by:

$$\delta T = T_{ms} - T_{cf} \quad (2.4)$$

Here  $T_{ms}$  is the temperature in the measurement section as measured by one of the sensors TI-126, TI-127 or T-128 and  $T_{cf}$  is the temperature in the cross-flow as measured by sensor TI-104. The standard deviation in  $\delta T$  can be estimated from the signal in figure 2.6 as:

$$\sigma_{\delta T} = \left( \frac{n}{n-1} \right)^{\frac{1}{2}} \left( \frac{1}{n} \sum (\delta T_i - \Delta T)^2 \right)^{\frac{1}{2}} \quad (2.5)$$

$n$  in represents the number of measurements:  $n=120$ .  $i$  indicates the time step over which is summated.  $\Delta T$  is defined as the mean of  $\delta T$ :

$$\Delta T = \frac{1}{n} \sum \delta T_i. \quad (2.6)$$

The standard deviation,  $\sigma_{\delta T}$ , is computed for the signals in figure 2.6 for all sensors in the measurement section. For the three sensors,  $\sigma_{\delta T}$  is approximately 0.09 K. Assuming an independent measurement every second, the mean temperature  $\Delta T$  can be calculated more accurately. The standard deviation in the mean  $\Delta T$  can be estimated by:

$$\sigma_{\Delta T} = \left( \frac{1}{n} \right)^{\frac{1}{2}} \sigma_{\delta T} \quad (2.7)$$

For our two minute measurement,  $\sigma_{\Delta T}$  is calculated to be 0.008 K this is a quite small value. This shows that the small time scale fluctuations in the signal have little effect on the mean value.

From this analysis it looks as if the temperature is measured very accurately. A limiting factor for the accuracy of the sensors is however the discrete reading of the sensors (nearest scale division: 0.1 K) and possible systematic errors. These two sources of errors are evaluated by analyzing the results from an isothermal run at approximately 25 °C. This run was carried out during the PIV measurements as described in appendix A. During this run there is no steam injection but the cross-flow is present. The 120 minute run is cut in 60 time intervals of 2 minutes. For each interval,  $\Delta T$  is calculated according to formula 2.6. We now have 60 values for  $\Delta T$  for each temperature sensor in the measurement section.

From this data set of 60 values for  $\Delta T$ , The mean value,  $\mu_{\Delta T}$ , is a measure for systematic error at this temperature. Similar, from these 60 values of  $\Delta T$ , the standard deviation,  $\Omega_{\Delta T}$ , approximated. This gives an indication of the random errors in the values of  $\Delta T$ . The formulas for these variables are:

$$\Omega_{\Delta T} = \left( \frac{m}{m-1} \right)^{\frac{1}{2}} \left( \frac{1}{m} \sum (\delta T_j - \mu_{\Delta T})^2 \right)^{\frac{1}{2}} \quad (2.8)$$

and,

$$\mu_{\Delta T} = \frac{1}{m} \sum \Delta T_j. \quad (2.9)$$

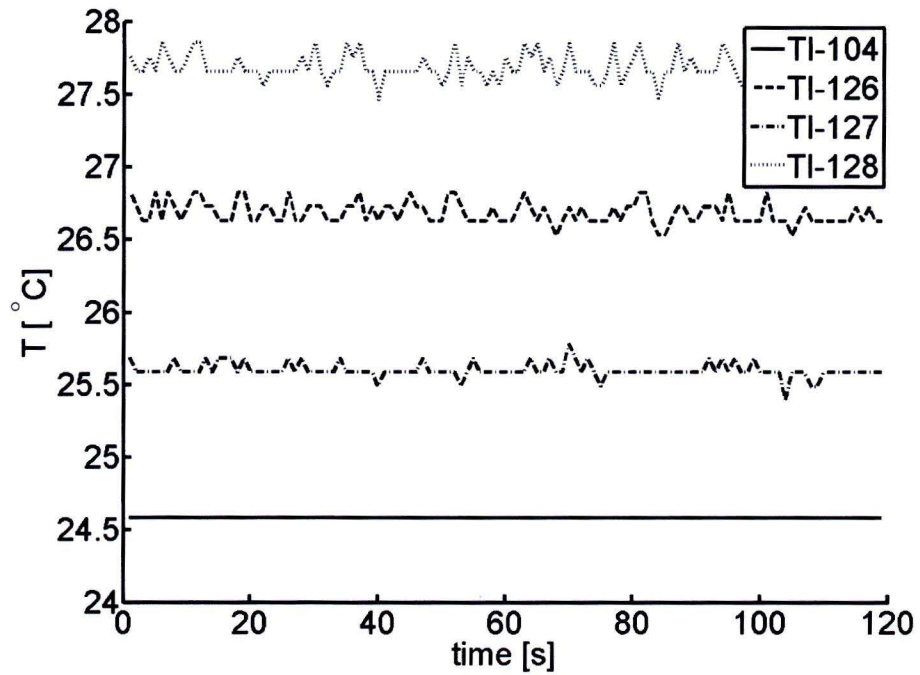


Figure 2.6: signal of the temperature sensors during one of the measurements with a cross flow temperature of approximately 25 ° C (25\_e).

Table 2.1: Calculated mean value and standard deviation for  $\Delta T$  from 60 time intervals during an isothermal run

	TI-126	TI-127	TI-128
$\mu_{\Delta T}$ [K]	0.0042	-0.0140	0.0692
$\Omega_{\Delta T}$ [K]	0.0206	0.0400	0.0589



Here  $m$  is the number of measurements; 60 in our case.  $j$  is the index of the two minute measurement. The values of  $\mu_{\Delta T}$  and  $\Omega_{\Delta T}$  as calculated from the isothermal run are shown in table 2.1.

The largest  $\mu_{\Delta T}$  that is found for the sensors approximately 0.07 K while for  $\Omega_{\Delta T}$  this is 0.06 K. As the mean value of  $\Delta T$  should be zero for the isothermal run,  $\mu_{\Delta T}$  counts as an systematic error. The value of  $\Omega_{\Delta T}$  is much higher than the value of  $\sigma_{\Delta T}$ . In general, these two values should be the same unless the  $n$  measurements that are used to compute  $\Delta T$  are not independent. We must however remember that we are dealing here with a discrete signal that has a discrete reading that is in the order of the fluctuations. Slow fluctuations (order of minutes) in the cross-flow temperature cause high random errors in the calculated  $\Delta T$ .

It is assumed that random and systematic errors as calculated for the isothermal run are also present in the measurements that are used to obtain the temperature fields. so, neglecting,  $\sigma_{\Delta T}$ , the total error in temperature can be found by adding up the values for  $\mu_{\Delta T}$  and  $\Omega_{\Delta T}$ . We estimate the error in  $\Delta T$  therefore to be:  $\varepsilon_{Temperature} = 0.13$  K.

## 2.4 Analysis

Temperature-difference fields are obtained for three different settings of the cross-flow temperature. The described temperature-difference field from figure 2.5 is a typical example of how the temperature field looks like for a cross-flow with a temperature of 25 °C. Figure 2.7 shows the  $\Delta T$  for a set of measurements that is performed with a cross-flow of 65 °C but otherwise the same settings. The same jet is present but  $\Delta T$  is lower. There is now a plume of high  $\Delta T$  on the left side of the domain. For the sets of measurements that were performed with a cross-flow of 75 °C,  $\Delta T$  of the jet is even lower and  $\Delta T$  of the plume is higher. This shows that a large portion of the heat that is supplied by the condensing steam is transferred to the cross-flow close to the steam injection point. Although the temperature of the jet is different for the figures 2.5 and 2.7, the trajectories of the jet center line look the same.

In figure 2.8 three temperature-difference fields are shown with different injection speeds but equal momentum ratio.  $\Delta T$  is not the same for the different temperature fields. The shape of the jet is however quite similar. The same is observed for other momentum ratios and temperatures of the cross-flow. Higher momentum ratios lead to an increasing penetration depth of the jet. The Cross-flow temperature seems to have only a minor effect on the penetration depth of the jet.

In the remainder of this section, the phenomena that are described here are investigated further.

### 2.4.1 Jet temperature center line

The temperature measurements are performed along three lines. Each sensor is translated along a line with an angle of 40 ° to the horizontal during a set of measurements. The highest local maximum along these lines is determined. The location of this maximum represents a point on the jet centerline.

The locations on the centerline are shown in figure 2.9, 2.10 and 2.11 for measurements at 25 °C, 65 °C and 75 °C respectively. Locations from the same temperature field are connected by a line. Each temperature field is represented by its unique combination of line style, marker type, and color. The meaning of the different attributes is explained in table 2.2. This way of depicting the data for the different temperature fields is used in the remainder of this chapter.

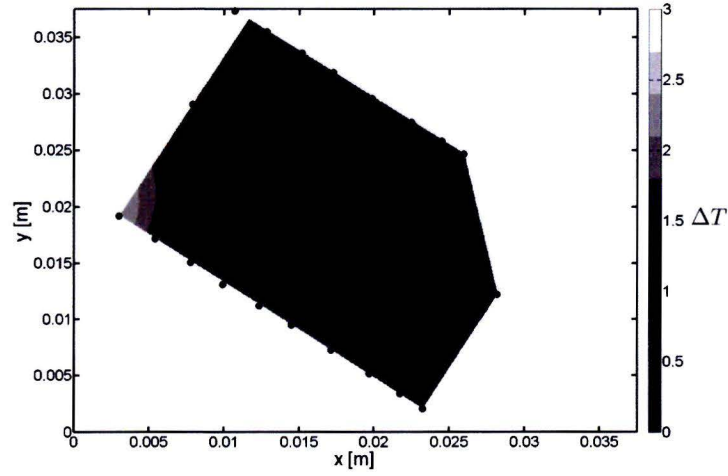


Figure 2.7: Temperature-difference field at 65 ° C for a steam mass flow of 1000 g/h and a cross flow of 0.95 m<sup>3</sup>/h (set 65\_e).  $\Delta T$  in Kelvin.

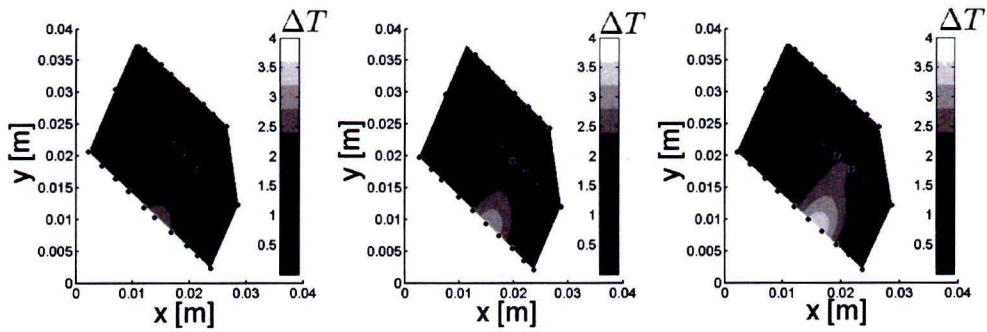


Figure 2.8: Temperature-difference fields at 25 ° at different steam injection speed but similar momentum ratio,  $J \approx 55$ .  $\Delta T$  in Kelvin. Left:  $m_{steam}=500$  g/h,  $Q_l=0.48$  m<sup>3</sup>/h (set 25\_d). Middle:  $m_{steam}=1000$  g/h,  $Q_l=0.95$  m<sup>3</sup>/h (set 25\_e). Right:  $m_{steam}=1500$  g/h,  $Q_l=1.41$  m<sup>3</sup>/h (set 25\_f).

Table 2.2: systematic indication of the measurement sets

Color	blue	red	green
$T_{cf}[K]$ °C	25	65	75
Marker type	○	▷	□
Steam mass flow [g/h]	500	1000	1500
Line Style	—	.....	- - - -
J	15	57	125

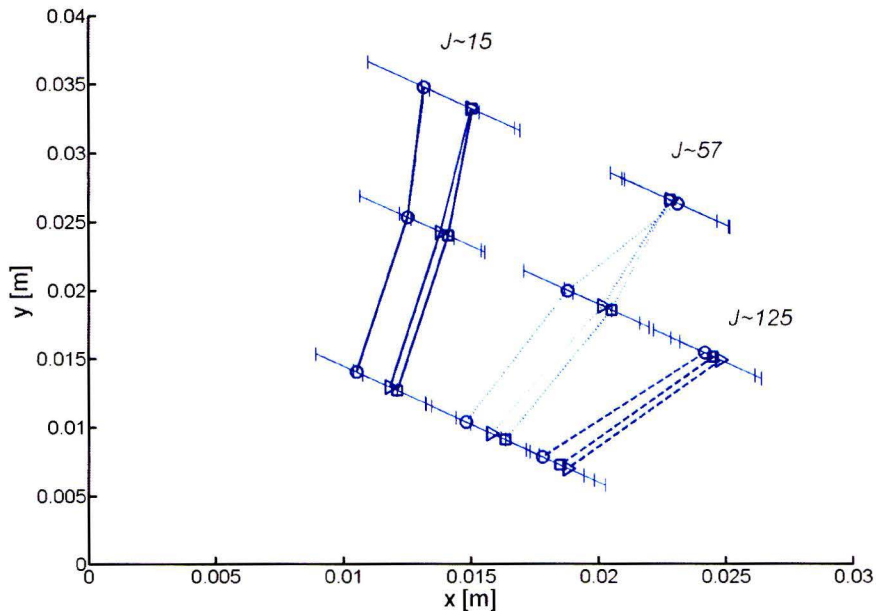


Figure 2.9: Jet temperature center lines at 25 °C for several combinations of momentum ratio and steam mass flow

Three kinds of errors play a role in determining the temperature center lines.

First, the location of the sample points is known with an accuracy of  $\varepsilon_{position} = \pm 0.5$  mm as described in section 2.3.

Second, there is only a limited number of sample points in a temperature field. The temperature field is determined with an interpolation spline. Supposing that this method can be compared with a linear interpolation, the maximum difference between estimation and the real profile would for a second order profile be half of the grid spacing. for our experiments this would be an error of  $\varepsilon_{discretisation} = \pm 1.4$  mm.

The last source of errors is introduced by the error in the temperature measurements. It was predicted in section 2.3 that the standard deviation in the value of  $\Delta T$  for one of the sensors amounts  $\Omega_{\Delta T} = 0.06$  K. To estimate the error in the position that this standard deviation causes,  $\varepsilon_{temp2distance}$ , we need to find a length scale that corresponds to this error. Half the width of the part of the jet is taken, that has a temperature that lies within 0.06 K of the maximum calculated temperature. This error is thus different for all measurements.

Together these three kinds of errors have been used to construct the error bars on the plots of the center lines. The total error is determined as:

$$\varepsilon_{centerline} = \sqrt{\varepsilon_{position}^2 + \varepsilon_{discretisation}^2 + \varepsilon_{temp2distance}^2} \quad (2.10)$$

The figures 2.9, 2.10 and 2.11 show that sets of measurements with the same momentum ratio,  $J$ , have almost the same temperature centerline trajectories. Jets with a higher momentum ratio penetrate further in the cross-flow. a outlier can be seen in figure 2.11.

The coordinates  $x$  and  $y$  can be scaled with  $rd$  according to formula (2.2). The scaled plots for the measurements with cross-flow temperatures 25 °C and 65 °C are presented in

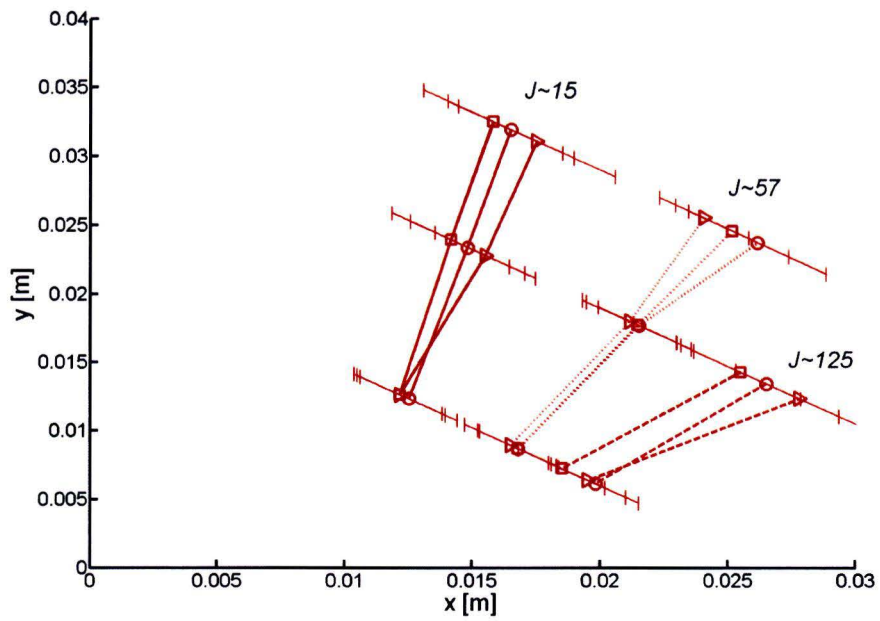


Figure 2.10: Jet temperature center lines at 65 °C for several combinations of momentum ratio and and steam mass flow

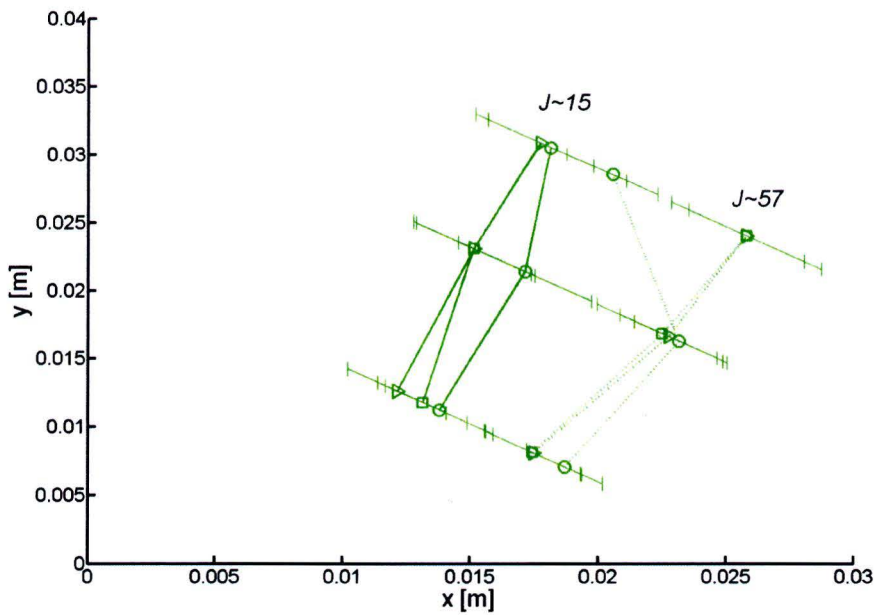


Figure 2.11: Jet temperature center lines at 75 °C for several combinations of momentum ratio and and steam mass flow

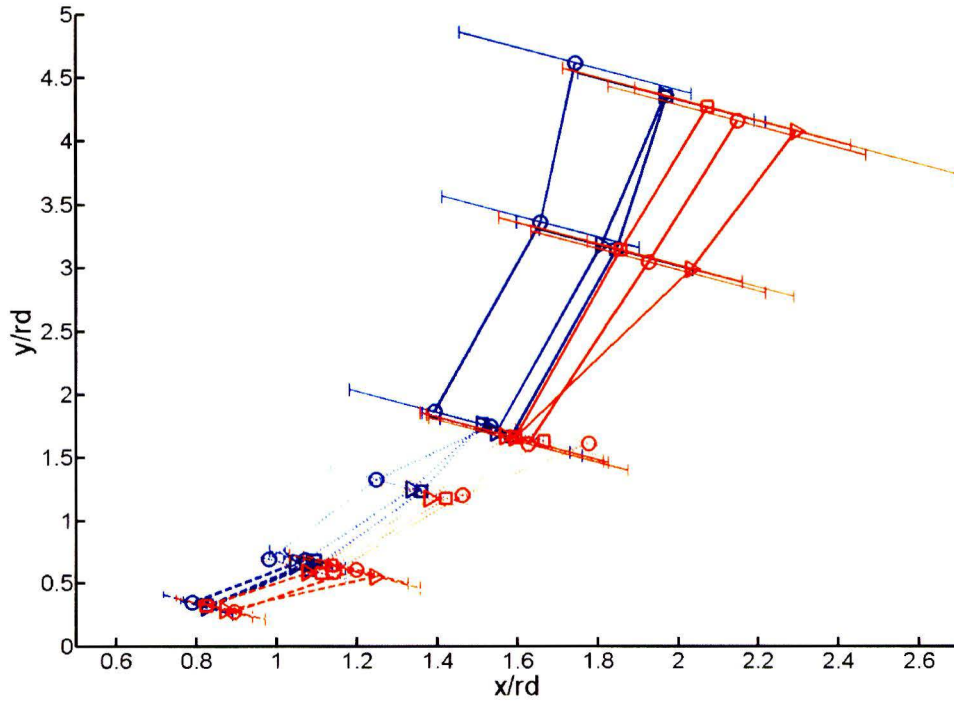


Figure 2.12: Dimensionless center line trajectories at 25 ° C and 65 ° C

figure 2.12. The scaling collapses the measurements with different momentum ratios towards a line that has the form of (2.2). We can determine the values for the parameters  $A$  and  $m$  with a least squares method with the Matlab curve fitting tool. Based on the all data points in figure 2.12,  $A = 1.3$  and  $m = 0.3$ . This is close to the values that Smith and Mungal [16] found. The difference can be caused by the different inlet conditions. For single phase measurements the inlet conditions are observed to influence the trajectories of the centerline. Thus for steam injection, the trajectories are expected to be different. It can be concluded that the temperature trajectory of the jet induced by the steam injection can be approximated quite well by single phase jets in cross-flows as found in literature.

#### 2.4.2 Jet maximum Temperature

The maximum value for  $\Delta T$  at the jet center line can be determined for all temperature fields. This maximum value for  $\Delta T$  can be lower than the temperature that is observed in the plume. As discussed in section 2.4.1 the value is evaluated along the lines of measurement and a local maximum is obtained.  $\Delta T_{max}$  is plotted as function of the distance along the jet axis:  $\xi$ . The value of  $\xi$  is estimated by integrating the fit for equation (2.2) for the center lines as determined in section 2.4.1 till it intersects the line of measurement. The results are shown in figure 2.13. The figure clearly shows that the temperature of the cross-flow has a large impact on  $\Delta T$ . A higher cross-flow temperature decreases  $\Delta T_{max}$ . Further more it can be seen that an increase in steam flow at a constant momentum ratio increases  $\Delta T_{max}$ .

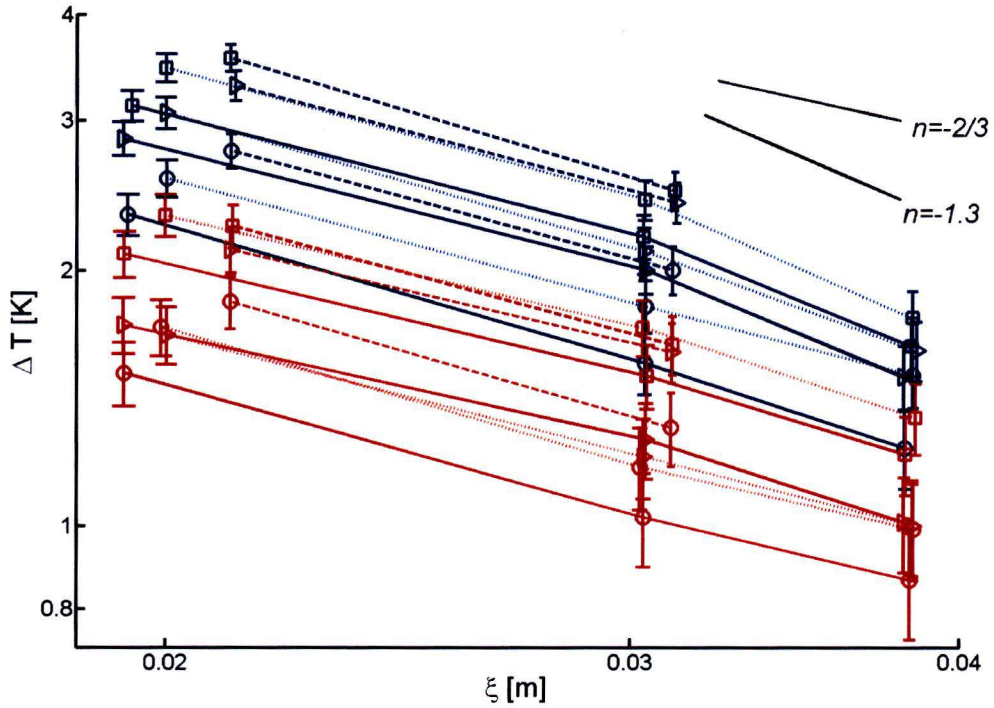


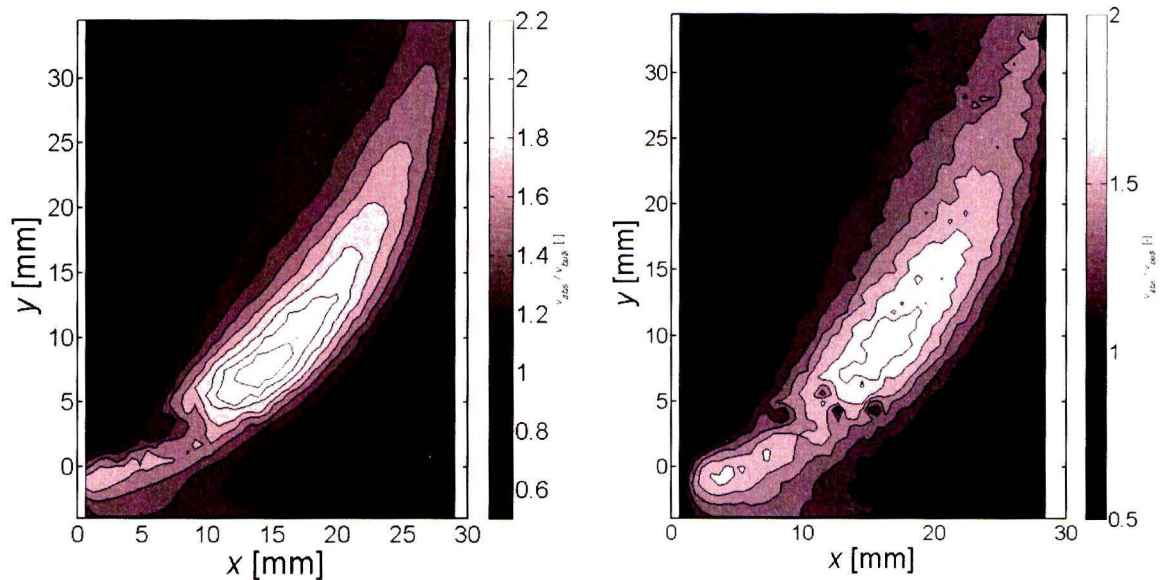
Figure 2.13: Temperature difference  $\Delta T$  at the center lines against the distance along the jet axis  $\xi$

Increasing momentum ratio also increases  $\Delta T_{max}$ .

In figure 2.13 a log-log scale is used to compare the decay with the one found by Smith and Mungal [16].  $\Delta T_{max}$  is supposed to be proportional to  $\xi^n$  with  $n = -1.3$  in the near field and  $n = -2/3$  in the far field. The transition from the near to the far field is expected at  $\xi_t = 0.3r^2d$  according to Smith and Mungal [16]. For the cases with  $J = 15$  the transition is predicted at  $\xi_t = 0.009$ . These center lines should be in the far field. For  $J = 57$  the transition is at  $\xi_t = 0.034$ . The transition is thus in the domain that is plotted. Finally for  $J = 125$ , the transition ought to take place at  $\xi_t = 0.075$ . These lines should therefore exhibit the behavior as expected in the near field.

In figure 2.13 two lines with  $n = -1.3$  and  $n = -2/3$  are plotted for comparison. The measurements are too inaccurate and the number of measurements is too low to distinguish between the values of  $n$  in the near and the far field that is expected. On the basis of the figure, it can be observed that  $n = 1 \pm 0.5$ . This doesn't contradict the observations by Smith and Mungal [16]

The expected error in  $\Delta T$ ;  $\varepsilon_{Temperature} = 0.13$  K, is indicated in the figure by the error bars. The error bars for small  $\Delta T$  are stretched because of the logarithmic scale.



(a) Cross-flow temperature of 25 °C,  $J = 57$  and steam mass-flux  $\dot{m} = 1000\text{g/h}$ . (25\_e) (b) Cross-flow temperature of 65 °C,  $J = 57$  and steam mass-flux  $\dot{m} = 1000\text{g/h}$ . (65\_e)

Figure 2.14: Velocity fields obtained with PIV measurements by Clerx [6]. The absolute velocity is scaled with the bulk velocity of the cross-flow.

### 2.4.3 Comparison with velocity fields

PIV measurements have been carried out by Clerx [6] to obtain the velocity profiles for conditions similar to the ones from the temperature measurements. The resulting velocity fields for a steam mass flow,  $\dot{m} = 1000 \text{ g/m}$  and an momentum ratio,  $J = 57$  are shown in figure 2.14 for a cross-flow temperature of 25 °C and 65 °C. Like for the temperature-difference fields, a jet is clearly visible. The velocity is not higher on the left side of the domain. This is a difference with the temperature-difference field for high cross-flow temperatures.

In figure 2.15, the center lines for  $\Delta T$  and velocity are plotted for a cross-flow temperature of 25 °C, a mass flow-rate,  $\dot{m}$ , of 1000 g/h and various momentum ratios. The temperature center lines do not penetrate as deep in the flow as the velocity center lines. The difference is smaller for higher momentum ratios. The difference between the velocity and temperature trajectories is also observed by Kamotani and Greber (1972) [9].

### 2.4.4 The plume

An interesting feature of the temperature-difference fields is the high temperature difference with the cross-flow,  $\Delta T$ , that occurs on the left side in some of the fields. As there is no velocity increase coupled with this phenomenon, it is called a plume in the following. In the figures 2.16 and 2.17 the fields for a cross-flow of 25 °C and 65 °C respectively are plotted ordered by steam mass-flow-rate and momentum ratio. With these figures, a qualitative analysis of the plume can be made. For a cross-flow temperature of 65 °C, a plume is visible for all temperature-difference fields. For the fields at 25 °C, only a very small plume can be observed

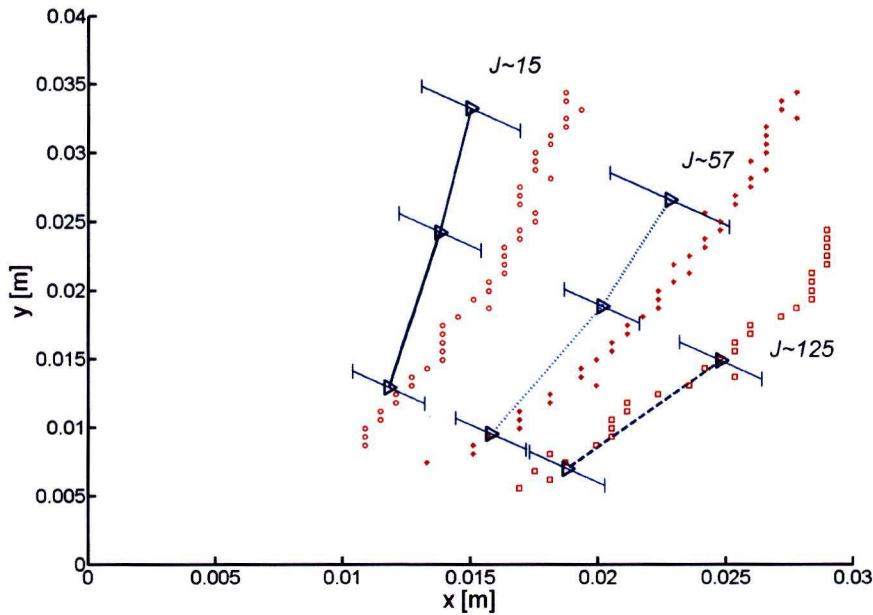


Figure 2.15: Comparison between the velocity center lines (red) and the temperature-difference center lines (blue) for cross-flow temperature  $25^{\circ}\text{C}$  and  $\dot{m}$  1000 g/h. momentum ratios,  $J$ , for the trajectories are indicated in the figure.

for low steam mass flow-rate. It can thus be concluded that the cross-flow temperature is the most important parameter, affecting the development of a plume. A possible explanation for the plume can be found in the way the injected steam condenses and interacts with the cross flow locally near the inlet. Clerx [6] describes the influence of cross-flow temperature and steam mass flux on the condensation of steam. Observations by Clerx are summarized in figure 2.1. For higher cross-flow temperature the penetration depth of a steam pocket is higher. The penetration depth of a steam pocket is defined here as the maximum distance the steam travels until it condenses. For a higher penetration depth, the evaporation occurs for a larger portion on the side than on the front of the steam pocket than is the case for a lower cross-flow temperature. It is assumed that this condensation on the side releases more heat to the cross flow. This causes the plume. Less heat is contained in the momentum carrying jet so  $\Delta T$  becomes lower. In figure 2.1 it is shown that a low steam mass flow also increases the penetration depth of the steam pockets but the effect of this parameter is not as strong as the cross-flow temperature. This influence of the steam mass-flow-rates on the penetration depth of steam pockets explains the small plumes that are observed for a steam mass flow of 500 g/h for a cross-flow of  $25^{\circ}\text{C}$ .

A more thorough investigation of the correlation between the penetration depth of the steam pockets and the existence of the plume would require temperature measurements at the left wall and a zoom-in on the injection point.

For completion, the temperature-difference fields for a cross-flow of  $75^{\circ}\text{C}$  is plotted in figure 2.18, for this cross-flow temperature, the plume is even more dominant than for the  $65^{\circ}\text{C}$ .



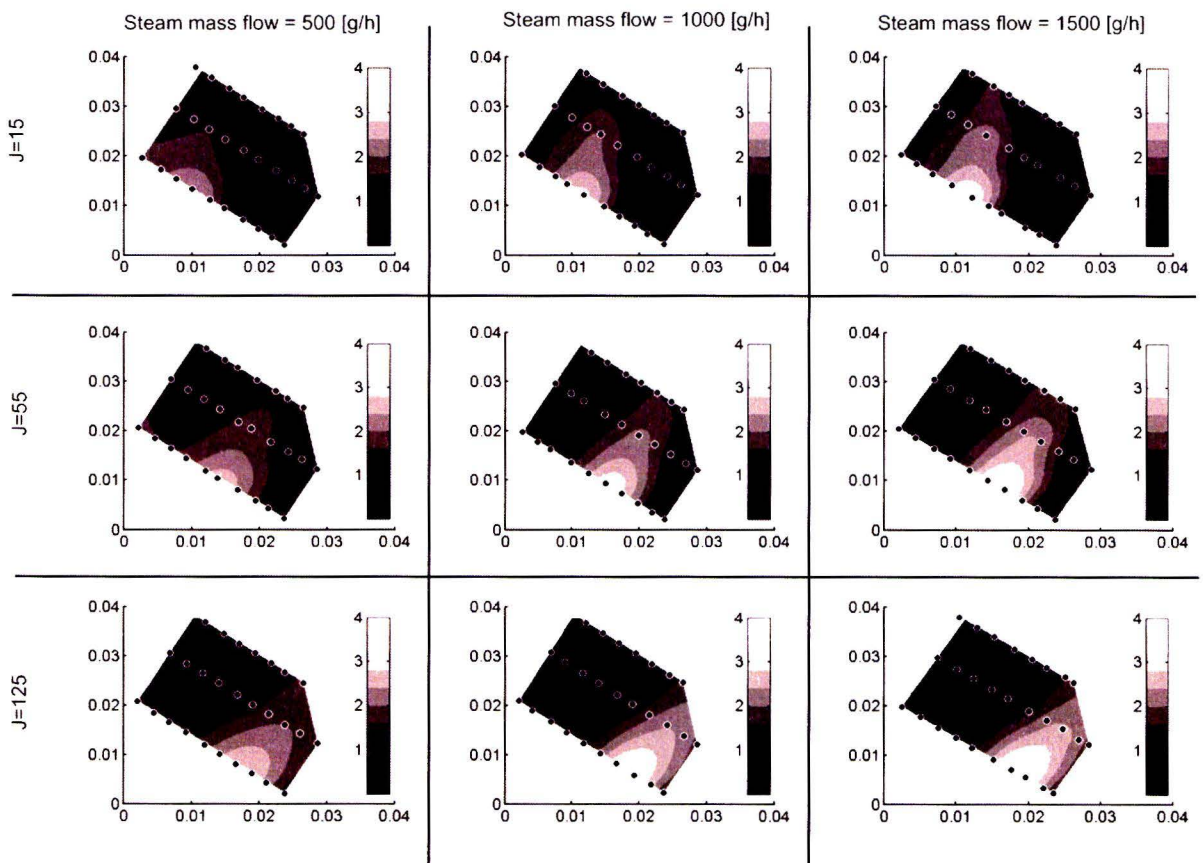


Figure 2.16: Temperature-difference fields at 25° C. The figures from left to right and from top till bottom show the measurement sets 25\_a till 25.i. Coordinates are x and y in m while the field values represent  $\Delta T$  [K].

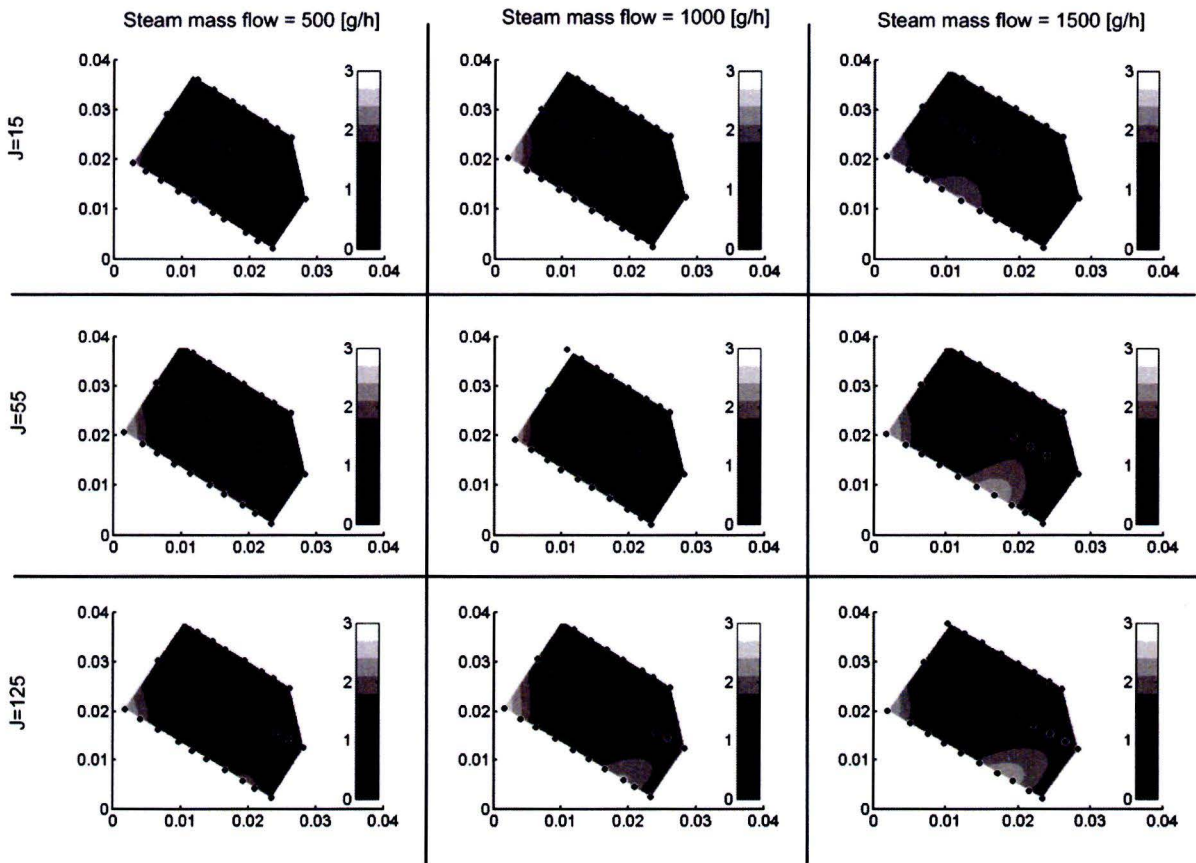


Figure 2.17: Temperature-difference Fields at 65° C The figures from left to right and from top till bottom show the measurement sets 65.a till 65.i. Coordinates are x and y in m while the field values represent  $\Delta T$  [K].

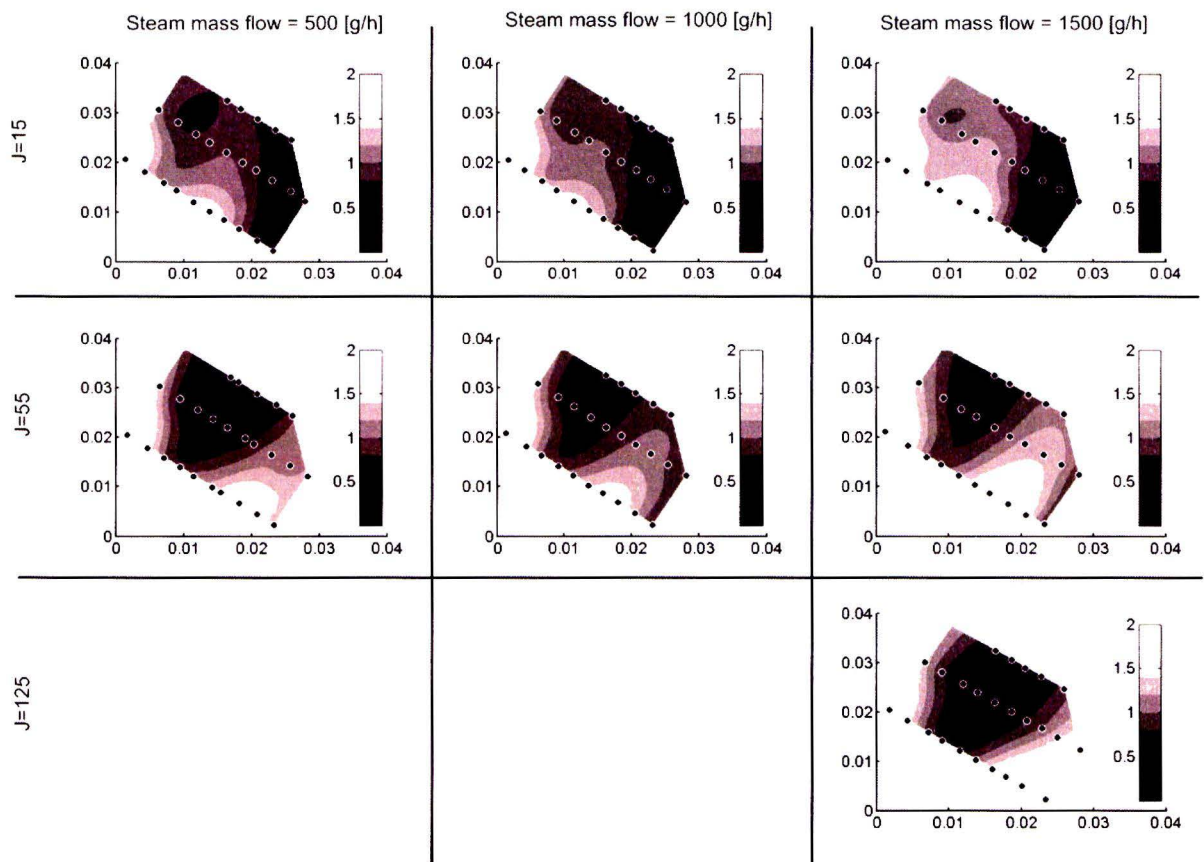


Figure 2.18: Temperature-difference Fields at 75° C The figures from left to right and from top till bottom show the measurement sets 75\_a till 75\_i. Coordinates are x and y in m while the field values represent  $\Delta T$  [K].

## Chapter 3

# Nonisothermal simulation of two phase flow with a diffuse interface model

For predicting the steam injection, a tool should be developed that is able to predict the flow consisting of water and steam including phase change. To make some first steps in the direction of such a model, a diffuse interface model for multi-phase flow is developed by Pecenko [15]. In this model the fluid is modeled as a Van der Waals fluid and surface effects were described as a function of the density gradient. DIM poses some requirements on the thickness of the interface that can be modeled. Because the interface thickness is larger near the critical point, ethane is modeled instead of water because at room temperature it is close to the critical point. In the model that is developed by Pecenko [15], no energy equation is present. In this chapter the model by Pecenko is extended with an energy equation and tested. This makes it possible to model the temperature effects, needed for a full description of multi-phase flows

The model that will be developed here is not meant as a ready tool for predicting steam injection. Rather, it is meant as a means of verifying new methods. Due to its form that describes the interface as a continuum with a large density gradient, the diffuse interface model that will be developed here will accurately describe the two phase behavior for some simple cases. Future tools that are able to describe more complex flows, with less stringent requirements on the thickness of the interface have still to be developed. These tools can be validated by the simple test cases presented in this chapter.

### 3.1 Diffuse interface method

To appreciate the strong and weak points of a diffuse interface method better it is easiest to compare it to its counterpart: a sharp interface model. In a sharp interface problem the fluid interface is modeled as a moving boundary with interfacial boundary conditions. Surface tension is modeled by a stress boundary condition. Boundary conditions for velocity are also applied. Mass transfer due to evaporation or condensation can also be described by interface boundary conditions. A method that works much like a free boundary model is the Volume of Fluid method as described by Liew [13]. VOF uses volume fractions to distinguish between phases. Although boundary conditions are included as a volumetric source term

in the governing equation they are clearly modeled from a sharp interface viewpoint. An advantage of VOF is that interface can be modeled by one or a few cells, regardless of the physical thickness that an interface would have under the given circumstances. This means that situations with very small surface thicknesses compared to the typical length scale can be modeled with VOF without a problem. For the application of VOF, free boundary conditions are necessary. If the free boundary conditions are specified wrong, this will off course lead to errors. The Diffuse interface method has the advantage that it avoids the need to apply these free boundary conditions.

In the diffuse interface method, the two phase system is modeled as a continuum without interfaces. An order parameter (density in our case) distinguishes between the two faces. Surface effects are dependent on the gradient of the order parameter. All other properties are correlated to the order parameter with a state equation and the proper thermodynamic relations. An advantage of this way of describing the fluid is that it does not involve that many approximations and assumptions. In DIM the physical interface should be captured with at least a couple of cells. This limits the use of DIM to cases with a small dimension and a thick interface. For this reason, DIM only functions close to the critical point.

## 3.2 The governing equations

To use the diffuse interface method, a set of equations is obtained that describe the behavior of the fluid in all possible states. The governing equations for the conserved quantities will be described first. Conserved quantities are mass, momentum and energy. The conservative equations differ from the ones for a single phase flow. Additional terms related to surface tension and surface energy are present. In diffuse interface methods, a state equation should be used that is accurate for both gaseous and liquid state. Relations between the density,  $\rho$ , specific internal energy,  $e$ , pressure,  $P$  and temperature,  $T$ , are based on the Van der Waals equation of state.

The mass, momentum and energy equation have a form that looks similar to the single phase equations. The mass density  $\rho$  is used to distinguish between gas and fluid phase. The extra energy and stresses due to the occurrence of surfaces are thus dependent on the gradient of  $\rho$ . The governing equations are written in conservative form so they can be used in a finite volume method easily. The conservation of mass can be described by the continuity equation for a compressible fluid:

$$\frac{\partial \rho}{\partial t} + \nabla \cdot (\rho \mathbf{u}) = 0 \quad (3.1)$$

Conservation of momentum is given by:

$$\frac{\partial \rho \mathbf{u}}{\partial t} + \nabla \cdot (\rho \mathbf{u} \mathbf{u}) = \nabla \cdot (\mathbf{d} + \mathbf{T}) \quad (3.2)$$

This is equivalent to the usual momentum equations but with an extra stress tensor  $\mathbf{T}$ . This is the so called Korteweg stress tensor and it models the surface forces.  $\mathbf{d}$  is the well known deformation stress tensor. The pressure gradient is included in  $\mathbf{T}$ . If we assume that there is no internal heat source, then the total energy equation becomes:

$$\frac{\partial(\rho E)}{\partial t} + \nabla \cdot (\rho E \mathbf{u}) = \nabla \cdot (\mathbf{u} \cdot (\mathbf{d} + \mathbf{T})) - \nabla \cdot \mathbf{q} - \nabla \cdot \mathbf{j}_E \quad (3.3)$$

With:

$$\rho E = \rho e + \frac{1}{2}|\rho \mathbf{u}|^2 + \frac{1}{2}K_E |\nabla \rho|^2 \quad (3.4)$$

Here in addition to the bulk internal energy,  $e$ , and the kinetic energy, a third form of energy is included. This is the surface energy and it is proportional to the density gradient squared. The constant,  $K_E$  is the gradient internal energy coefficient. As can be seen there is energy transfer due to both viscous,  $\mathbf{d}$ , and surface forces,  $\mathbf{T}$  acting on the fluid. Another means of energy transfer is by conduction with flux  $\mathbf{q}$ . The third energy flux,  $\mathbf{j}_E$  is a nonclassical flux that follows from the requirement that entropy of the system may not decrease and it is known as interstitial working. It can be viewed as an extra surface effect.

The equations for mass, momentum and energy can be found in Anderson and McFadden[1]. They are not in conservative form yet. Pecenko [15] has written the mass and momentum equations in conservative form. The energy equation can easily be written in the above form as is shown in appendix G.

The above equations need constitutive relations to complete the model. The heat flux is given by the Fourier law as

$$\mathbf{q} = -k \nabla T \quad (3.5)$$

Here  $k$  is the thermal conductivity of the fluid. For the deformation tensor, a Newtonian model with the Stokes assumption is used:

$$\mathbf{d} = -\frac{2}{3}\mu(\nabla \cdot \mathbf{u})\mathbf{I} + \mu(\nabla \mathbf{u} + (\nabla \mathbf{u})^T) \quad (3.6)$$

The Korteweg stress tensor  $\mathbf{T}$  consists of the well-known pressure and some terms that describe the surface forces as a function of the mass density and its derivatives:

$$\mathbf{T} = [-p + K\rho \nabla^2 \rho + \frac{1}{2}K|\nabla \rho|^2]\mathbf{I} - K\nabla \rho \otimes \nabla \rho \quad (3.7)$$

In this way  $\rho$  fulfills the role of the order parameter by relating surface effects to changes in its values.  $K$  is the gradient energy coefficient. Anderson and McFadden (1996) [2] show that  $K$  in the Korteweg tensor can be replaced by  $K_e$  for reversible surface effects and a constant gradient energy coefficient. They show that the non-classical heat flux takes the form:

$$\mathbf{j}_E = K_E \frac{D\rho}{Dt} \nabla \rho = K_E (\rho \nabla \cdot \mathbf{u}) \nabla \rho \quad (3.8)$$

This term ensures that entropy is not decreasing. We make the heat conductivity  $k$  and the viscosity  $\mu$  dependent on the mass density in the following way:

$$\mu = c_1 \rho \quad (3.9)$$

$$k = c_2 \rho \quad (3.10)$$

This choice is arbitrary. It was chosen like this to account for the higher heat conductivity and viscosity in the liquid phase. More advanced models could also take into account temperature effects. The value for  $K$  has to be held constant because this is one of the conditions for the derivation to be valid. Obviously the set of equations is not complete yet. An equation for the pressure and the temperature will be derived from state equations. To do this, a relation for the internal energy of a Van der Waals fluid has to be found. This will be described next. It can be seen that the gravity force has not been taken in account. Gravity related phenomena are neglected. The length scales that are used here will be too small for gravity to play a role in the physical behavior.

### 3.2.1 An approximation of the internal energy for a fluid described by a Van der Waals equation of state

The pressure of a fluid can be expressed as a function of the mass density and the temperature by the Van der Waals equation. According to the CRC handbook of chemistry and physics [12] the Van der Waals equation reads:

$$(P + n^2a/V^2)(V - nb) = nRT \quad (3.11)$$

For the pressure, the following equation now holds:

$$P = \frac{RT}{M\nu - b} - \frac{a}{M^2\nu^2} = \frac{RT}{M - b\rho} - \frac{a}{M^2}\rho^2 \quad (3.12)$$

A general expression for the internal energy is derived in Çengel [5] based on the Gibbs relations and the Maxwell relations:

$$e_2 - e_1 = \int_{T_1}^{T_2} c_v(T, \nu_1) dT + \int_{\nu_1}^{\nu_2} \left[ T \left( \frac{\partial P(T, \nu)}{\partial T} \right)_{\nu} - P(T, \nu) \right]_{T_2} d\nu \quad (3.13)$$

If one uses the pressure according to the Van der Waals equation in the second part of the right hand side of the equation for the internal energy this term becomes:

$$\int_{\nu_1}^{\nu_2} \left[ T \left( \frac{\partial P(T, \nu)}{\partial T} \right)_{\nu} - P(T, \nu) \right] d\nu = \int_{\nu_1}^{\nu_2} \frac{a}{M^2\nu^2} d\nu = \frac{a}{M^2}(-1/\nu_2 + 1/\nu_1) = \frac{a}{M^2}(\rho_1 - \rho_2) \quad (3.14)$$

In Çengel [5], a general relation for the specific heat of a substance for constant volume,  $c_v$ , can be found:

$$\left. \frac{\partial c_v}{\partial \nu} \right|_T = T \left. \frac{\partial^2 P}{\partial T^2} \right|_{\nu} \quad (3.15)$$

Substituting the Van der Waals equation in this formula yields:

$$\left. \frac{\partial c_v}{\partial \nu} \right|_T = 0 \quad (3.16)$$

The specific heat will thus depend on temperature only. This is different from what is observed for real substances. For real substances  $c_v$  tends to differ between the two phases. Other state equations might be able to present a better dependence of the specific heat on the density. For low mass density and high temperature, the Van der Waals equation approximates an ideal gas. It is reasonable to expect that for low density, the specific heat can be modeled by that of an ideal gas. Like the specific heat of a Van der Waals fluid, that of an ideal gas only depends on temperature. As there is no dependence of  $c_v$  on the density for a Van der Waals gas, the specific heat of the Van der Waals fluid will be the same as that for an ideal gas. If one makes the assumption of a constant specific heat, the temperature can be written as a function of internal energy and density.

$$T = T_0 + \frac{1}{c_v}(e - e_0) - \frac{a}{M^2 c_v}(\rho_0 - \rho) \quad (3.17)$$

The subscript 0 indicates a reference state. This state can be chosen arbitrarily. For our case the critical point is chosen because fluid properties at the critical point are well known.

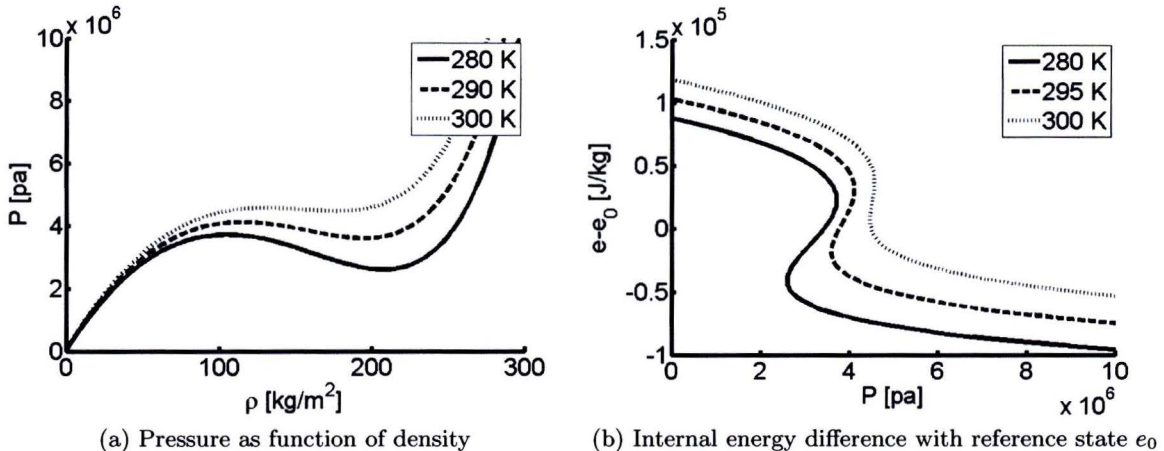


Figure 3.1: Physical properties of a Van der Waals fluid near the critical point at constant temperatures. For the properties of the fluid, those of ethane have been chosen:  $a = 0.558 \text{ Pa m}^6 \text{ mol}^{-2}$ ,  $b = 6.51e - 5 \text{ m}^3 \text{ mol}^{-1}$ ,  $M = 0.03, \text{ kg/mol}$ ,  $c_\nu = 1489.7 \text{ J kg}^{-1} \text{ T}^{-1}$ ,  $T_0 = 305.5 \text{ K}$ ,  $\rho_0 = 203.2 \text{ kg m}^{-3}$

For ethane the Van der Waals constants and the molar mass can be found in The CRC handbook of chemistry [12]. The specific heat has been chosen as the specific heat for the ideal gas at 300 K. The physical behavior near the critical point is shown in figure 3.1. A two phase region is present. For certain values of the pressure and temperature there is no unique corresponding value of the density. For temperatures closer to the critical point the two phase region becomes flat and at the critical temperature the two phase region disappears. In figure 3.1b the effect of isothermal evaporation can be seen. At a single value of the pressure the internal energy can make a jump to a higher level. This shows the effect of evaporation.

### 3.3 The Numerical method

In the previous section the governing equations have been discussed. The system consists of partial differential equations in conservative form, (3.1), (3.2), (3.3), and two algebraic state equations, (3.12),(3.17). There are a couple of unknown variables;  $\rho, p, e, T$  and a velocity component for every spatial dimension. The system is closed as there are as many unknowns as equations. In appendix F the system of equations is written for two dimensions. A numerical method can be used to calculate the time dependent solution, provided that we specify initial conditions. In the simulations that are presented in the remainder, initial conditions for  $\rho, T$  and  $\mathbf{u}$  are specified. The conservative form of the equations makes it possible to apply a finite volume method without adaptations to the system of equations. A cell centered formulation of the Finite volume method is used. We use a two dimensional simulation for the bulk of our simulations. This means that the grid points represent the center of a quadrilateral cell. Spatial discretisation in this form reads:

$$\frac{d}{dt} \mathbf{U}_{i,j} = \frac{1}{\Delta x} \left( \mathbf{F}(\mathbf{U})_{i+\frac{1}{2},j} - \mathbf{F}(\mathbf{U})_{i-\frac{1}{2},j} \right) + \frac{1}{\Delta y} \left( \mathbf{G}(\mathbf{U})_{i,j+\frac{1}{2}} - \mathbf{G}(\mathbf{U})_{i,j-\frac{1}{2}} \right) \quad (3.18)$$



Here  $\mathbf{U}_{i,j}$  represents the vector of conserved variables in the grid point  $(i, j)$  while  $\mathbf{F}(\mathbf{U})$  and  $\mathbf{G}(\mathbf{U})$  are the vectors of the fluxes in  $x$  and  $y$  direction. These flux vectors are determined by discretizing the part of the differential equations that is behind the divergence operator at the edges of the quadrilateral cells. For the two dimensional equations as described in appendix F, The flux  $\mathbf{F}(\mathbf{U})$  is equal to the terms that are differentiated with respect to  $x$ . For  $\mathbf{G}(\mathbf{U})$  the same holds but now for the terms that are differentiated with respect to  $y$ . The values of the variables at the edges of the cell are found by a second-order accurate interpolation.

$$u_{i+\frac{1}{2},j} = \frac{1}{12}(-u_{i-1,j} + 7u_{i,j} + 7u_{i+1,j} - u_{i+2,j}) \quad (3.19)$$

The first and second order derivatives are discretized in these points by:

$$\left. \frac{\partial u}{\partial x} \right|_{i+\frac{1}{2},j} = \frac{1}{\Delta x}(u_{i+1,j} - u_{i,j}) \quad (3.20)$$

$$\left. \frac{\partial^2 u}{\partial x^2} \right|_{i+\frac{1}{2},j} = \frac{1}{2(\Delta x)^2}(u_{i-1,j} - u_{i,j} - u_{i+1,j} + u_{i+2,j}) \quad (3.21)$$

A time integration method is needed to evaluate the left hand side of equation (3.18). The  $p/\rho$  plot has a negative compressibility in a part of the domain. This compressibility is un-physical. In this region, a small perturbation would lead to phase separation. This intrinsic instability could lead to numerical instabilities. To increase the stability, A Total Variation Diminishing Time integration scheme is used. Shu and Osher [17] show that such a scheme can significantly increase stability. A third-order accurate TVD-Runge-Kutta time scheme algorithm is used as described by Cockburn and Gau [7]. By denoting the r.h.s. of 3.18 as  $\mathbf{A}(\mathbf{U})_{i,j}$  the time integration scheme reads

$$\mathbf{U}_{i,j}^{(1)} = \mathbf{U}_{i,j}^{(n)} + \Delta t \mathbf{A}(\mathbf{U}^{(n)})_{i,j} \quad (3.22a)$$

$$\mathbf{U}_{i,j}^{(2)} = \frac{3}{4}\mathbf{U}_{i,j}^{(n)} + \frac{1}{4} \left[ \mathbf{U}_{i,j}^{(1)} + \Delta t \mathbf{A}(\mathbf{U}^{(1)})_{i,j} \right] \quad (3.22b)$$

$$\mathbf{U}_{i,j}^{(n+1)} = \frac{1}{3}\mathbf{U}_{i,j}^{(n)} + \frac{2}{3} \left[ \mathbf{U}_{i,j}^{(2)} + \Delta t \mathbf{A}(\mathbf{U}^{(2)})_{i,j} \right] \quad (3.22c)$$

The pressure and the temperature are updated every stage using the algebraic state equations (3.12) and (3.17).

### 3.4 One-dimensional simulations

A one dimensional simulation of the model is performed to check the behavior of the simulations and to compare it to an analytical analysis. The behavior of the simulations is compared with a so called 'isothermal model'. This later model has no equation for the energy. Rather than calculating the temperature from an energy equation, the temperature is assumed to be constant. In this model the only unknowns are  $\rho$ ,  $\mathbf{u}$  and  $p$ . The continuity equation (3.1), momentum equation (3.2) and the Van der Waals equation (3.12) are the only equations in this model. Simulations with this model have been carried out by Pecenko [15]. The total model as described in section 3.2 will in the remainder be denoted by the 'non-isothermal model'.

The initial density is chosen in the unstable regime. A small initial disturbance will grow exponentially in time. The analytical behavior for both the isothermal and the non-isothermal model can be compared. First the governing equations are linearized around the reference state in the unstable region by the following substitutions.

$$\rho(x, t) = \rho_i + \epsilon \hat{\rho} \exp(i(\beta x - \omega t)) \quad (3.23)$$

$$u(x, t) = \epsilon \hat{u} \exp(i(\beta x - \omega t)) \quad (3.24)$$

and

$$T(x, t) = T_i + \epsilon \hat{T} \exp(i(\beta x - \omega t)) \quad (3.25)$$

Here  $\rho_i$  and  $T_i$  represent the initial mass density and temperature. The perturbation parameter  $\epsilon$  is chosen small such that linearization is justified.  $i$  is the imaginary unit,  $\beta$  is the real wave number and  $\omega$  is the complex angular frequency. A positive imaginary part of  $\omega$  indicates a growing amplitude while a negative imaginary part yields a decreasing amplitude. The relation between  $\beta$  and  $\omega$  for a set of equations can be found by removing all terms from the equation that are not linear in  $\epsilon$ . This leads to a solution of the form.

$$\epsilon \exp(i(\beta x - \omega t)) \mathbf{A}(\beta, \omega) \begin{bmatrix} \hat{\rho} \\ \hat{u} \\ \hat{T} \end{bmatrix} = 0. \quad (3.26)$$

For the equation to hold the determinant of the matrix  $\mathbf{A}$  should be zero. Calculation of the determinant yields an expression for  $\omega$ . For the isothermal model, the zero determinant condition leads to a quadratic equation for  $\omega$ :

$$\omega^2 + \frac{4}{3} i \nu_i \beta^2 \omega - \alpha \beta^2 - \rho_i K \beta^4 = 0. \quad (3.27)$$

As before, the subscript  $i$  is used to indicate the value of a property at the initial state. The kinematic viscosity  $\nu$  is used.

$$\alpha = \left( \frac{\partial p}{\partial \rho} \right)_{T,i}$$

is used to simplify the written equation.  $\alpha$  represents a measure for the compressibility of the fluid at constant temperature.

In the unstable part of the phase diagram, one of the solutions for the angular frequency has a positive imaginary part. This means that the perturbation will grow exponentially at first. After a finite time, perturbations become larger and the linear equation doesn't hold anymore.

The extra equation for the Temperature that is present in the non-isothermal case leads to a more complex relation for  $\omega$ . The equation is now cubic:

$$\left( \omega^2 + \frac{4}{3} i \nu_i \beta^2 \omega - \alpha \beta^2 - \rho_i K \beta^4 \right) (c_v \rho_i \omega + i k_i \beta^2) - \frac{T_i}{\rho_i} \zeta^2 \omega \beta^2 = 0. \quad (3.28)$$

with

$$\zeta = \left( \frac{\partial p}{\partial T} \right)_{\rho,i}.$$

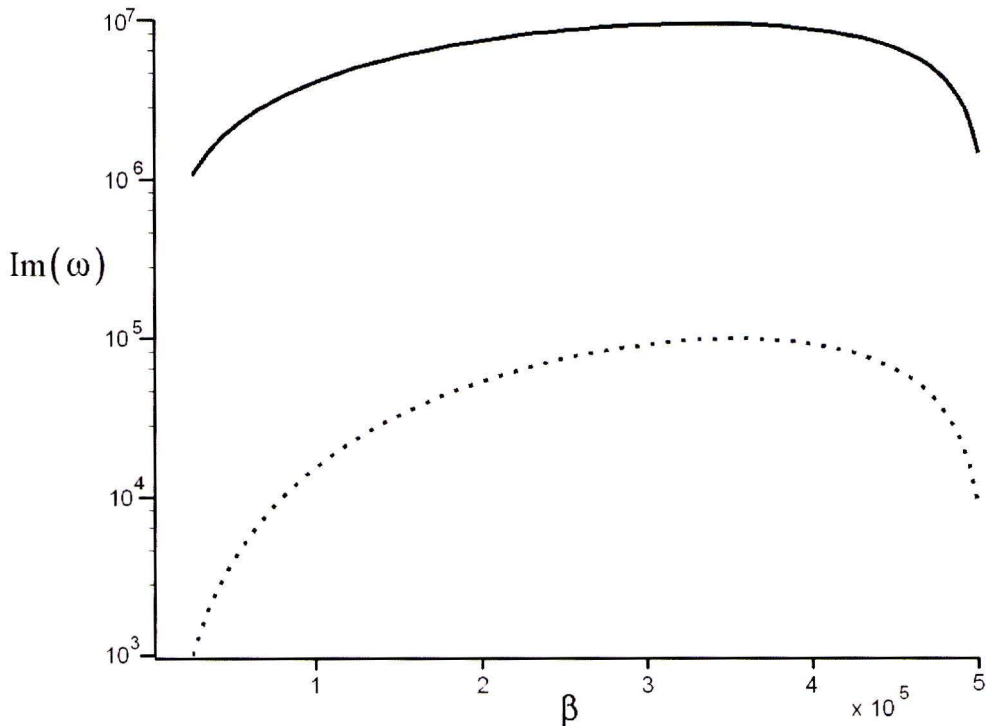


Figure 3.2: Imaginary part of the complex angular frequency for the most unstable eigen mode. The solid line represents the 'isothermal' case. The dotted line represents the 'non-isothermal' case

Note that the first term between parentheses is the determinant in the isothermal case. It follows that when either the specific heat  $c_v$  or the heat conduction coefficient  $k_i$  is very large, the stability behavior of the non-isothermal and isothermal cases is the same. This is not surprising, since a large specific heat or a large heat conduction coefficient both lead to approximately constant temperature. Also when  $\zeta$  is small the pressure is hardly influenced by a change in temperature and the equation for temperature is effectively decoupled from the other two equations.

In most situations, the last term in (3.28) is important and a difference between the stability analysis can be observed between the isothermal and the non-isothermal situation. For specified fluid properties and initial conditions a stability analysis can be made by plotting the highest imaginary part of  $\omega$  as function of the wave number. In figure 3.2 this has been plotted for an isothermal and a non-isothermal model for an ethane-like fluid with a temperature close to the critical temperature and an initial density chosen in the unstable region of the phase diagram.

As is clear from the figure, both cases have an unstable mode. According to the equations, the most unstable perturbation for the isothermal model grows 100 times faster than the non-isothermal one. One dimensional simulations have been performed to verify this behavior. A simulation with an initial density in the unstable region as described in appendix E is chosen. The density has an initial perturbation. The behavior of both the isothermal and the non-isothermal response to the perturbation is shown in figure 3.3. The growth of the initial disturbance is much faster for the isothermal simulation (there is a factor 100 difference in

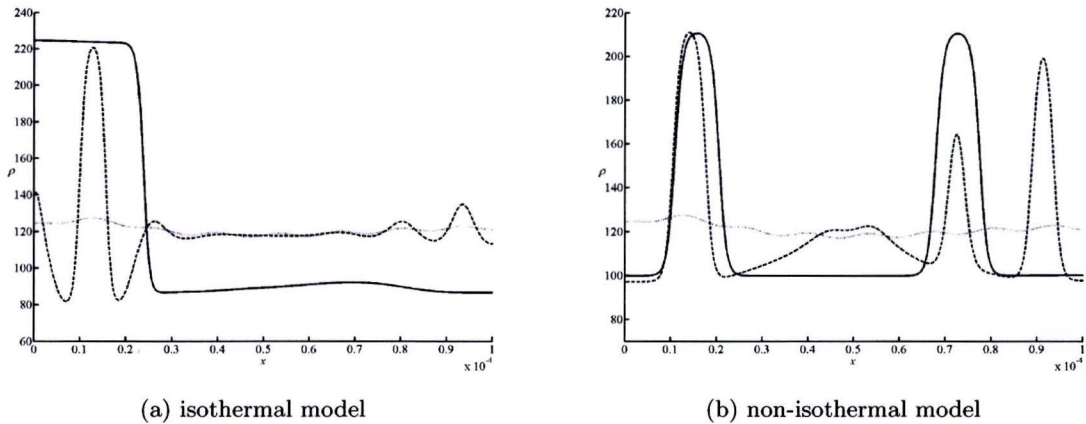


Figure 3.3: Phase separation for a one dimensional simulation that starts from a perturbed unstable initial density (dotted line). The mass density profile is shown for some random time steps for both isothermal and non-isothermal model.

simulation time). Also coalescence of the initial 'drops' evolves much faster for the isothermal simulation. At the final time step, the isothermal simulation shows a single drop at the right side of the domain while the non-isothermal simulations has still two drops that show no tendency to merge. Taking in account the energy equation thus makes the phase separation process slower as shown analytically. It also seems to prevent movement of the drop interfaces through the fluid. From a physical point of view this can be understood. In the isothermal case, for an interface means that locally the density has to change. This can be induced by a difference in mass flowing to the interface from one side and the mass that flows out on the other side. A drop that consists of two interfaces in one dimension can thus propagate easily through the domain by fluid flow induced by surface forces. The same propagation of the interface for the non-isothermal model would also require the density to change locally. But the compression of the fluid would lead to a higher local temperature and pressure. The movement of the interface would thus be counter-acted by a pressure rise. For a one dimensional simulation this restricts movement of the drops quite severely.

A one dimensional condition with a specified wave number is performed to validate the numerical method. Growth rate at small amplitudes is compared to the predicted value based on the value for  $\omega$  that is calculated with equations 3.27 and 3.28. The growth rates calculated from the simulations correspond very well to the ones predicted by the analytical expressions. A description and the results of these simulations can be found in appendix H

### 3.5 Two-dimensional simulations

Two dimensional simulations have been performed for several phenomena involving liquid drops in gas. The non-isothermal model as described in section 3.2 is implemented with the numerical method that is explained in section 3.3. A square domain with a Cartesian grid is used. Symmetry boundary conditions are implemented on all four edges of the domain. The initial condition for the cases we present here is symmetrical in both horizontal and vertical

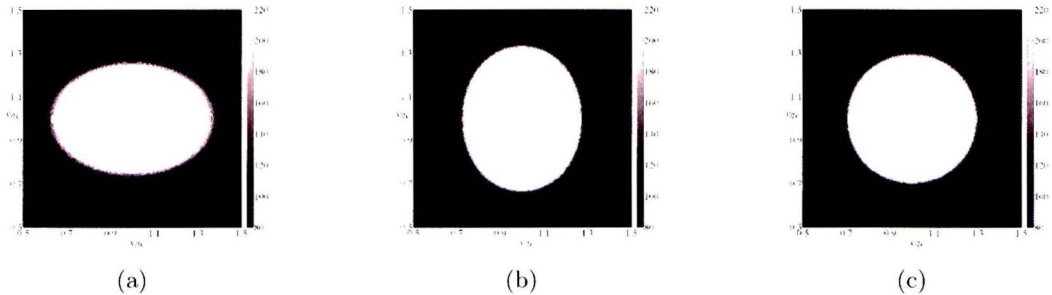


Figure 3.4: Mass density profile,  $\rho$  [kg/m<sup>3</sup>] for the drop retraction simulation for a 400<sup>2</sup> grid (case Mb). The density field is shown at the initial state, a, intermediate state, b, and final state, c.

direction. Because the solution is assumed to remain symmetrical the simulations have been performed on a quarter of the domain saving computational time. Three types of phenomena are presented here. In the drop retraction problem the initial solution is an elliptical drop. The drop evaporation problem starts from a circular drop but here the temperature of the surrounding gas is higher than that of the drop. In the drop collision case two drops of the same size collide on each other. The three cases are used to validate the numerical method. A full description of all performed 2 dimensional simulations and their settings can be found in appendix E The length of the numerical domain is indicated by  $lx$  in the following. Note that due to symmetry that has been applied, the actual domain has a length of  $2lx$

### 3.5.1 Drop retraction

The drop retraction case is used to validate the method. The initial state in this case is an elliptical drop surrounded by vapor. To prescribe the initial density in a continuous way, a formulation with a hyperbolic tangent function is used:

$$\rho(x, y) = \rho_{av} - \Delta\rho \tanh\left(\frac{(x - x_0)^2 + 2(y - y_0)^2 - R_0^2}{\delta}\right). \quad (3.29)$$

Here  $\sqrt{\delta}$  represents the thickness of the interface and  $R_0$  is a measure for the drop dimensions. The length of the drop along the x-axis is  $\sqrt{2}$  times larger than that along the y-axis. Temperature is set constant at 290 Kelvin for the entire field and the initial velocity is set to zero. A square domain is used with dimensions  $2 \cdot 10^{-4}$  m by  $2 \cdot 10^{-4}$  m. The drop center is located in the middle of the domain.

The drop starts oscillating between two elliptical states and eventually, the oscillations are damped by viscous effects. This results in a circular final state. The solution for the density of the simulation is shown in figure 3.4 for three instances of time. This behavior is as expected. The effect of surface tension leads to a minimization of the drop surface (circumference in our case) thus leading to a eventual circular drop.

The radius of the drop in x and y direction are plotted as functions of time in figure 3.5. To calculate this radius, the location of the interface is evaluated as the position where the density is the same as the average of that of the fluid and the liquid phase. A damped oscillation is visible in the figure.

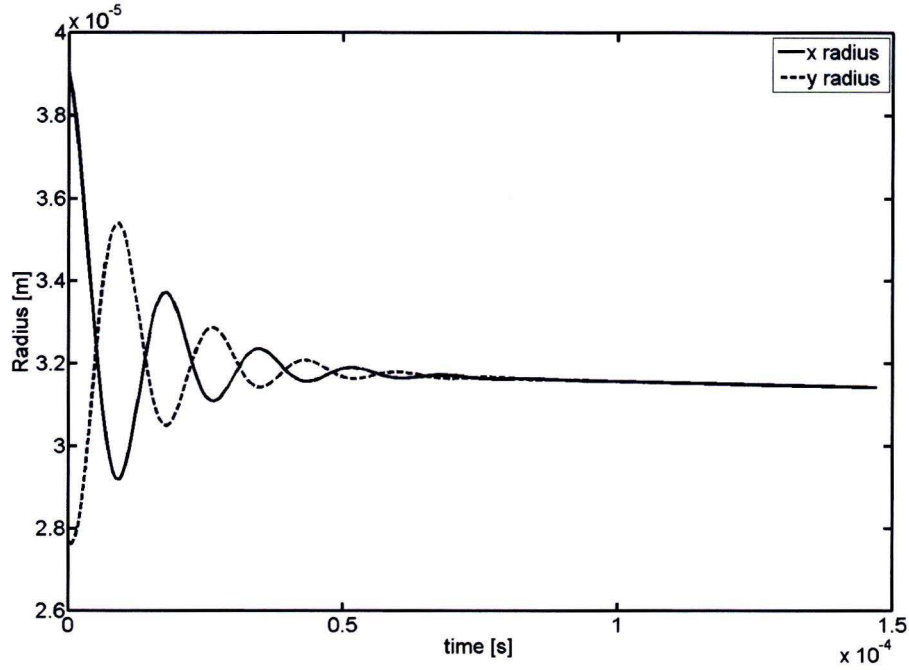


Figure 3.5: Drop retraction simulation. Evolution of drop dimensions along x and y-axis for a drop retraction case on a  $400^2$  grid (CaseMb)

### Conservative variables

To check the implementation of the non-isothermal DIM method, we study the conservation of the mass and energy. The nature of the equations, boundary conditions and the finite volume method that is applied should ensure a perfect conservation of the total mass and energy for the entire domain. This is easily verified by computing the total mass and energy in the domain. To check the performance of the simulations, the case of an ecliptic drop is used to demonstrate mass and energy conservation. To quantify the error in conservation of total mass and energy, the relative error is used. The relative error is defined as:

$$\varepsilon_{relative} = \frac{Y_n - Y_0}{Y_0} \quad (3.30)$$

Here  $Y$  is the total of the conserved property summed over the numerical domain and the subscripts 0 and n indicate the initial and an arbitrary time step respectively.

It can be seen that the relative error in the mass is of order  $1 \cdot 10^{-15}$  while that of the energy is of the order  $1 \cdot 10^{-13}$ . The error in the energy equation increases the first iterations and then remains constant in time. A good explanation for this behavior is not found but the explanation can most likely be found in the way the initial condition is prescribed. The relative errors of both energy and mass are so small that rounding off errors are the most likely cause. This shows that the implementation of the finite volume method and the boundary conditions works as expected.

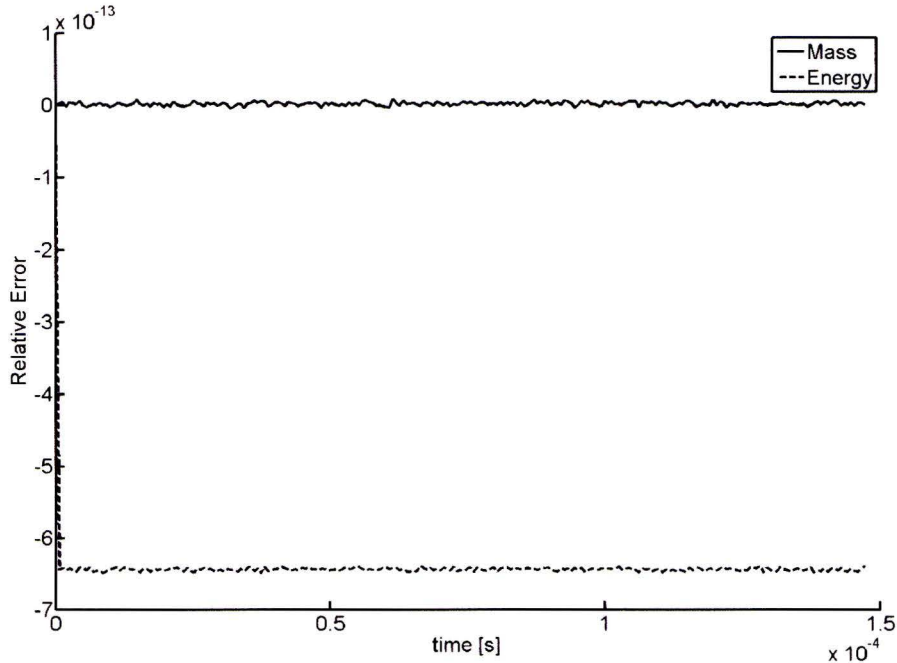


Figure 3.6: Relative error in the conservation of the total mass and energy for the drop retraction simulation (case Mb)

### Convergence

It is important that the numerical method converges to a unique solution for smaller grid spacings. If this would not be the case, the method would be nonphysical because the grid spacing should play no role in the exact solution that would be obtained for an infinite number of grid points. Simulations similar to the one discussed before ( $400^2$  grid points) have been performed but now with  $200^2$  and  $800^2$  points. The cases are labeled Ma ( $200^2$ ), Mb ( $400^2$ ) and Mc ( $800^2$ ). The Courant number is taken constant to avoid instabilities. The used time step is thus proportional to the grid spacing.

The radius measured along the x-axis is shown in figure 3.7 for the three cases. The three grids yield similar results and the lines for the two finest grids almost overlap. This shows that the solution for the elliptical problem converges nicely to a unique solution. A Richardson extrapolation is used to approximate the 'true' value for a grid with an infinite number of grid points. The Richardson extrapolation is defined according to Heath [8] as:

$$Q_R = Q(\Delta x) + \frac{Q(\Delta x) - Q(\Delta x/q)}{q^{-p} - 1} + O(\Delta x^{p+1}) \quad (3.31)$$

Here  $\Delta x$  is the grid spacing,  $Q$  is the value calculated numerically for a variable.  $q$  represents the grid refinement parameter. This is the ratio between the two grids.  $q$  is 2 if we compare for example the grids from case Ma and Mb.  $p$  is the order of accuracy of the numerical method. Our numerical method is second order accurate ( $p = 2$ ). The Richardson extrapolations for the radius, based on cases Ma and Mb, and the cases Mb and Mc are plotted in figure 3.7. The difference between the two Richardson extrapolations is larger than expected. This is

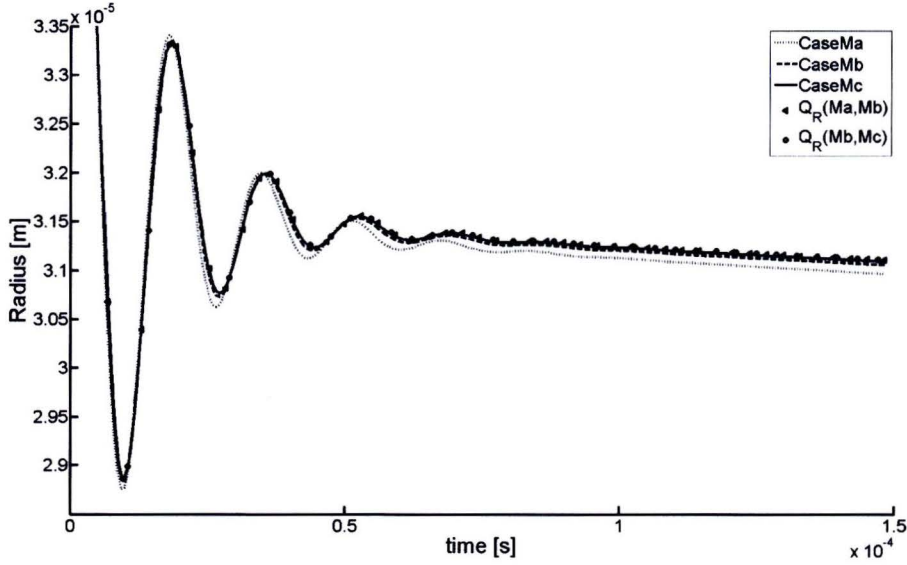


Figure 3.7: Grid convergence for drop retraction simulations. The figure shows the evolution of the radius in x direction for the cases with  $200^2$  (Ma),  $400^2$  (Mb) and  $800^2$  (Mc) grid points. The Richardson extrapolation  $Q_R$  based on cases Ma and Mb, and the cases Mb and Mc are also plotted.

probably due to the way the boundary conditions are implemented. The size of the domain will increase slightly for finer grid spacings. This leads to a lower order accuracy that is expected from the discretisation of the equations.

### Surface tension

An interesting feature of the two phase method is that it takes into account surface tension. This surface tension is the driving force behind the deformation of the elliptical drop. The final state is a circular drop. In this final state the surface tension induces a pressure difference between the liquid and the vapor. The pressure inside the drop will be higher than outside. The pressure difference can be calculated as:

$$\Delta p = \frac{\sigma}{R}, \quad (3.32)$$

$\sigma$  represents the surface tension and  $R$  represents the radius of the drop. The surface tension at the final stage is evaluated along the x-axis and along the diagonal. There is a small difference between the two values. This is because the drop has a slightly non-circular shape due to the Cartesian grid that has been used. The value of the surface tension according to (3.32) has been calculated to be  $\sigma = 0.29493 \pm 1.88 \cdot 10^{-3}$ .

The theoretical value of the surface tension can be calculated as

$$\sigma = \sqrt{2} \int_{\rho_1}^{\rho_2} [K \Delta F(\rho)]^{\frac{1}{2}} d\rho, \quad (3.33)$$

where  $\Delta F(\rho)$  denotes the Helmholtz free energy density that results when a unit volume of a mixture of liquid and its saturated vapor with average mass density  $\rho$  is converted into



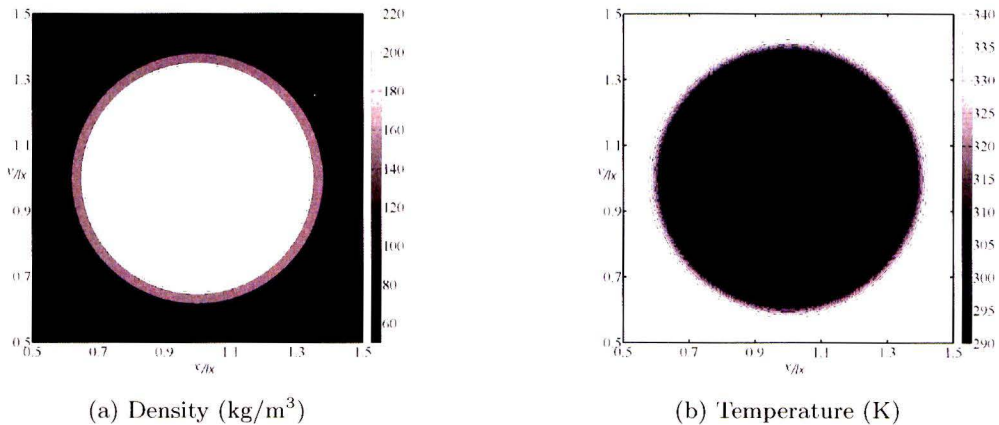


Figure 3.8: Initial conditions for the drop evaporation simulation (case H).

a uniform phase of the same density (Cahn 1959 [4]). The value of the final temperature and the densities are used to compute the analytical value for the surface tension. This yields:  $\sigma = 0.29718$ . This corresponds very well to the value for the surface tension that was calculated based on (3.32). In Appendix J, a description is provided of the calculation of the surface tension.

### 3.5.2 Drop evaporation

An advantage of the non-isothermal model compared to the isothermal one as described by Pecenko [15] is the possibility to model the effects of temperature differences and heat transfer. A particular interesting case is that of an evaporating drop. Evaporation of a drop can be demonstrated with a simple simulation. The drop evaporation case involves heat transfer and phase change and is thus an interesting study case for the non-isothermal model.

The initial state of the simulation is a circular drop in the center of a square domain. Density and temperature are prescribed with a hyperbolic tangent function similar to (3.29). The temperature inside the droplet is set to 290 K and the pressure is set to the saturation pressure at this temperature. Temperature, pressure and density inside the drop are thus the same as the ones used in the drop retraction cases described in section 3.5.1. The initial temperature of the surrounding vapor is set to 340 K and the pressure is set to the same value as inside the drop. This means that the gas is superheated. The initial conditions for the density and the temperature are shown in figure 3.8. Details on the settings for the simulation can be found in appendix E.

The evolution of the density profile is shown in figure 3.9. The density is shown for some arbitrary time steps. The drop shrinks and eventually totally disappears due to evaporation. Plots of the density and the temperature along the x-axis are shown in figure 3.10 and 3.11. The domain is plotted from the boundary to the center. It can be seen that the density and temperature inside the drop remain approximately constant at the initial value while the drop shrinks. This is a result of the choice to prescribe saturated conditions inside the drop. Outside the drop, the temperature drops due to heat flow towards the interface. At the same time the density of the gas increases due to the evaporation of the liquid.

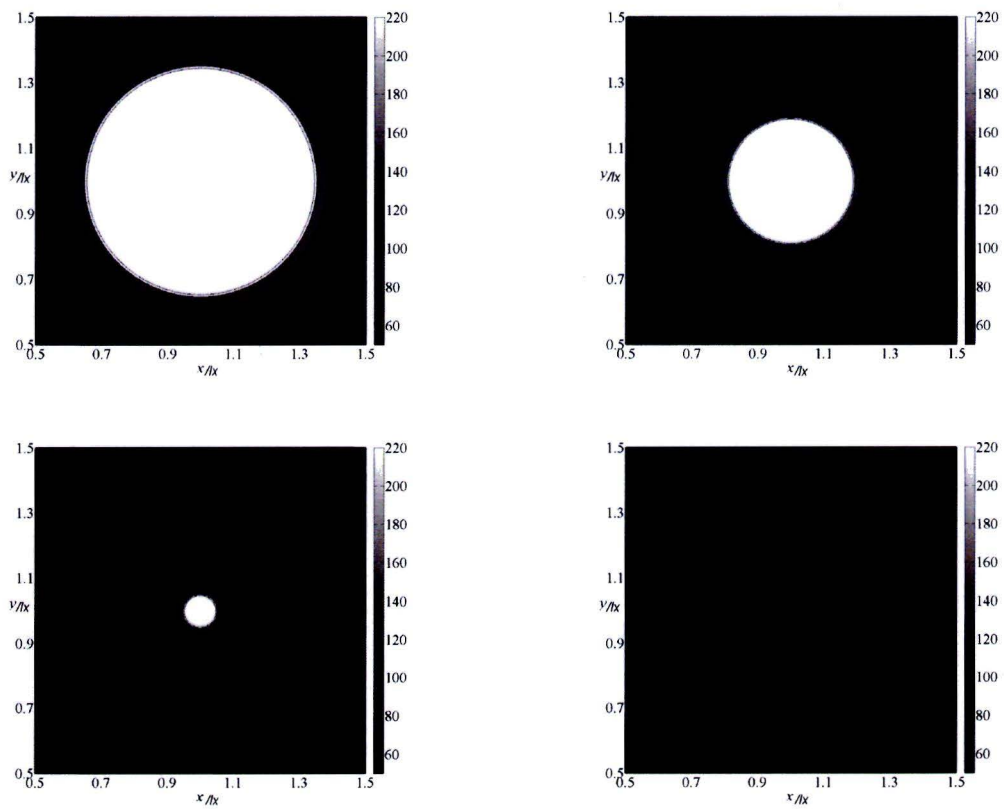


Figure 3.9: Density [ $\text{kg/m}^3$ ] field for the drop evaporation simulation (case H) at several times.

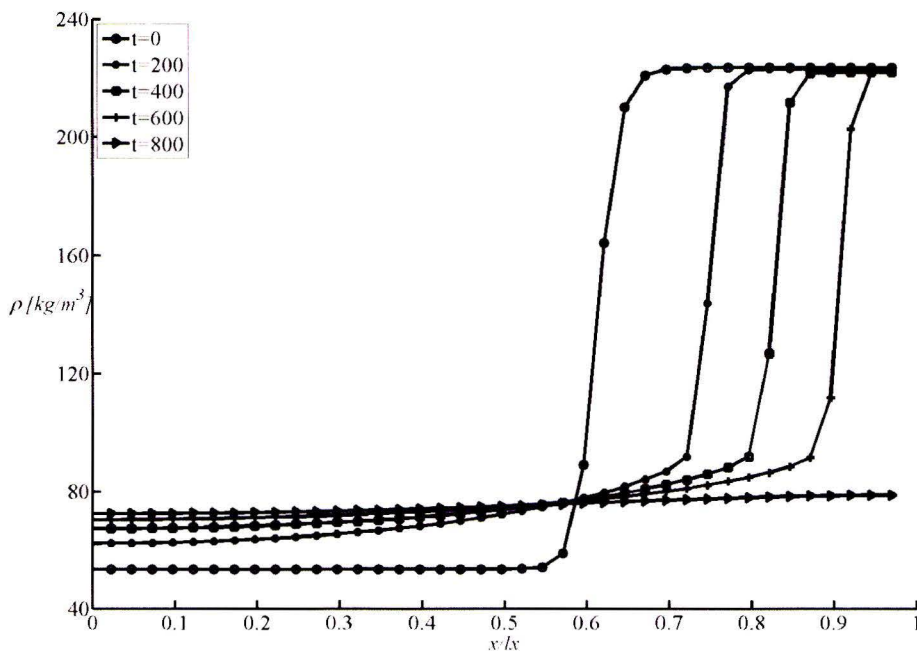


Figure 3.10: Density plotted along the x-axis trough the center of the drop for the drop evaporation simulation (case H). The density profile is plotted for several instances of time.

### 3.5.3 Drop collision

The case of two colliding drops can be used to investigate surface dynamics. Various phenomena can be observed. Locally the surface can merge, break up or just remain unaltered. The influence of these phenomena on two colliding drops can lead to several types of behavior. In some cases drops have found to bounce, where in other cases they just coalesce. Drop breakup has been observed as well as inclusion of small gas bubbles. For the simulations, the speed of the drops and the heat conductivity has been varied. Two drops of the same size and same but opposite initial velocity are simulated. The drops are initially placed a little bit apart and the velocity is uniform in the drops while zero outside. This setup makes it possible to perform simulations on a quarter of the domain. An overview of the collision simulations and a complete description is found in appendix E. We will characterize the cases here by their Weber number and their Prandtl-number. The Weber-number is defined as (Ashgriz and Poom [3])

$$We = \frac{\rho_l V^2 D}{\sigma},$$

with  $D$  the diameter of the drop.  $V$  is the relative velocity of the two drops. For our case this means that  $V$  is two times the velocity of one of the drops. The Weber number gives the ratio of the kinetic to the interfacial energy. For our simulations, the Weber number will only change as function of velocity. This number is a good indicator for the drop dynamics but for local phenomena like coalescence and breakup it is insufficient because phase change occurs locally near the interface. The Prandtl-number is therefore used as a second characteristic

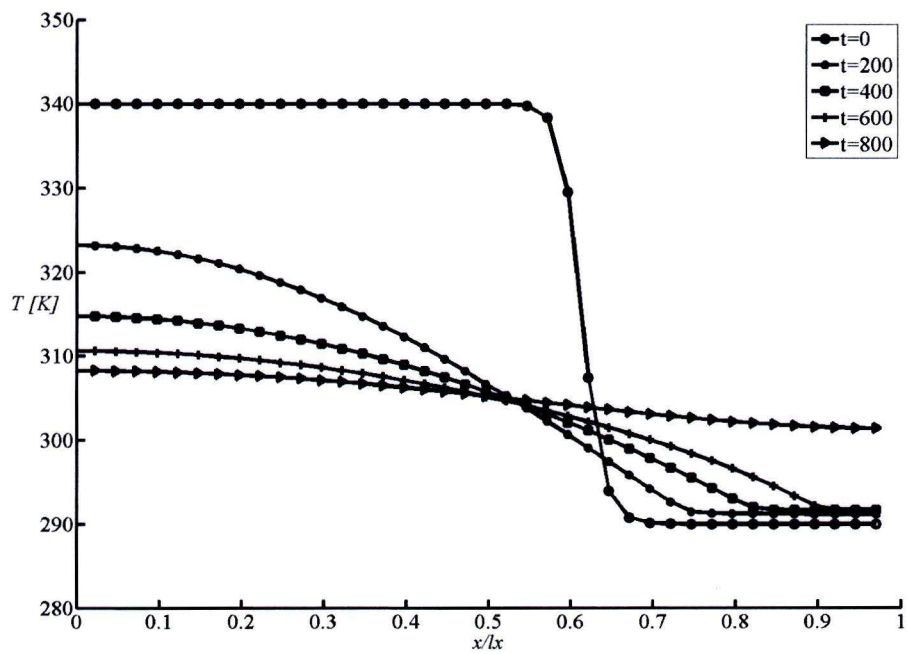


Figure 3.11: Temperature plotted along the  $x$ -axis trough the center of the drop for the drop evaporation simulation (case H). The Temperature profile is plotted for several instances of time.

number for drop colision. The Prandtl-number is defined by:

$$Pr = \frac{c_p * \mu}{k},$$

We use the  $c_p$  that can be obtained for an ideal gas that has the same properties as the Van der Waals fluid that we use here. Because  $k$  and  $\mu$  are both proportional to the density, this definition will lead to a unique value for the Prandtl-number for a simulation. For simulations with  $Pr = 1$ , Figures 3.12, 3.13 and 3.14 show the effect of different  $We$ . For all three cases the drops coalesce. The Weber number influences mostly the elongation of the droplet after it is formed. As can be seen, the maximum stretch that occurs is higher for higher  $We$ . For the largest Weber number (figure 3.14) the elongation becomes so large that the drop coalesces with the upper and bottom wall. Because of the symmetry boundary conditions, this is numerically equivalent with coalescence with a droplet on the other side of the wall. The stretched drop breaks up and a small drop forms in the breakup zone. This last mentioned drop is small and not stable. It disappears after some iterations.

In figures 3.15, 3.16 and 3.17 the results of simulations for  $Pr = 150$  are shown. To obtain a higher Prandtl-number the heat conductivity,  $k$ , of the simulation is chosen lower. For low Weber-number the drops bounce back as can be seen in figure 3.15. The drops do not get a chance to unite and the drops deform like a spring. As there is no connection between the drops, the two drops transform the 'spring energy' that is stored in them by deformation in kinetic energy. in this way the drops have a velocity opposite to the initial one. For higher Weber numbers, the drops do coalesce as can be seen in figure 3.16. For even higher Weber-numbers bubbles form inside the droplet. These bubbles are caused by entrapment of vapor. Before coalescence occurs, the drops are stretched and the coalescence does not occur only in the center but also at other places. This leads to the included drops that can be seen in figure 3.17. For this case in contrast to the case with the low Prandtl-number, the drop doesn't break up and coalesce with the side wall.

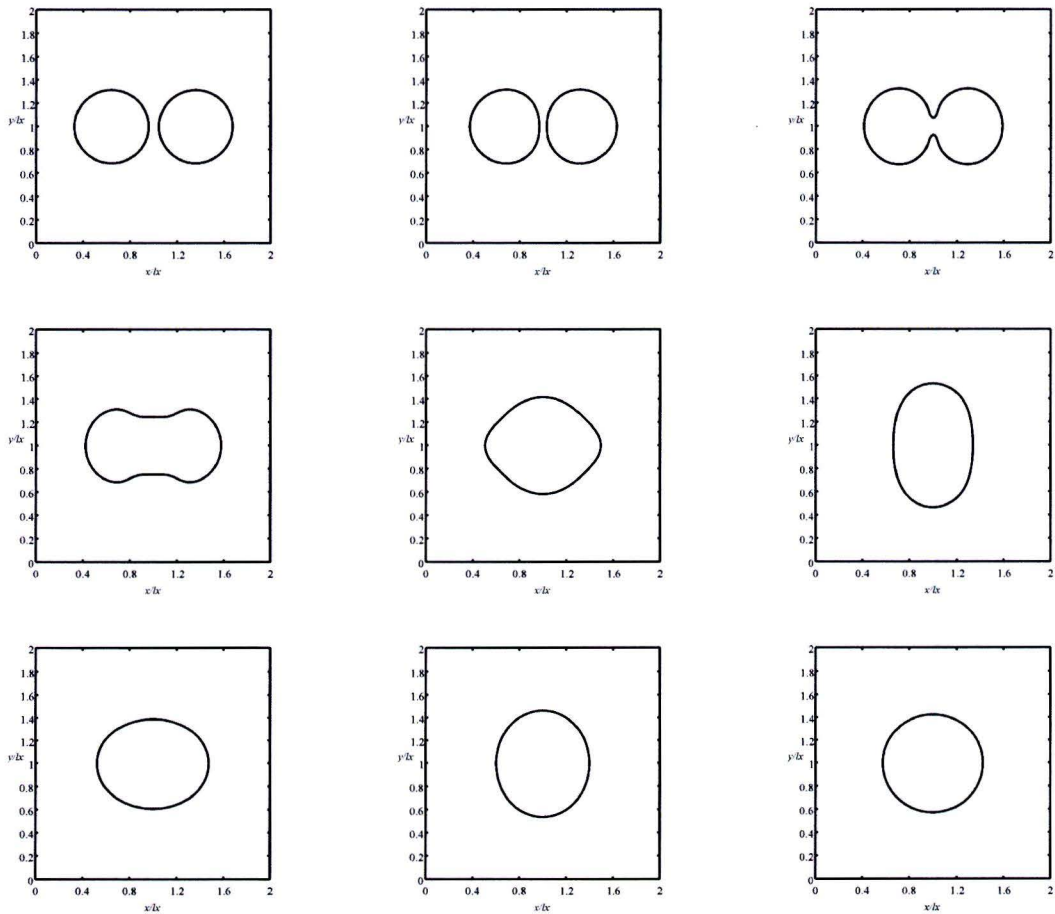


Figure 3.12: Two-dimensional drop collision simulation with  $Pr = 1$  and  $We = 1.19$  (Case Na). From left to right and top to bottom: time evolution of the simulation at arbitrary subsequent times. The isosurface of mass density is shown at the average.

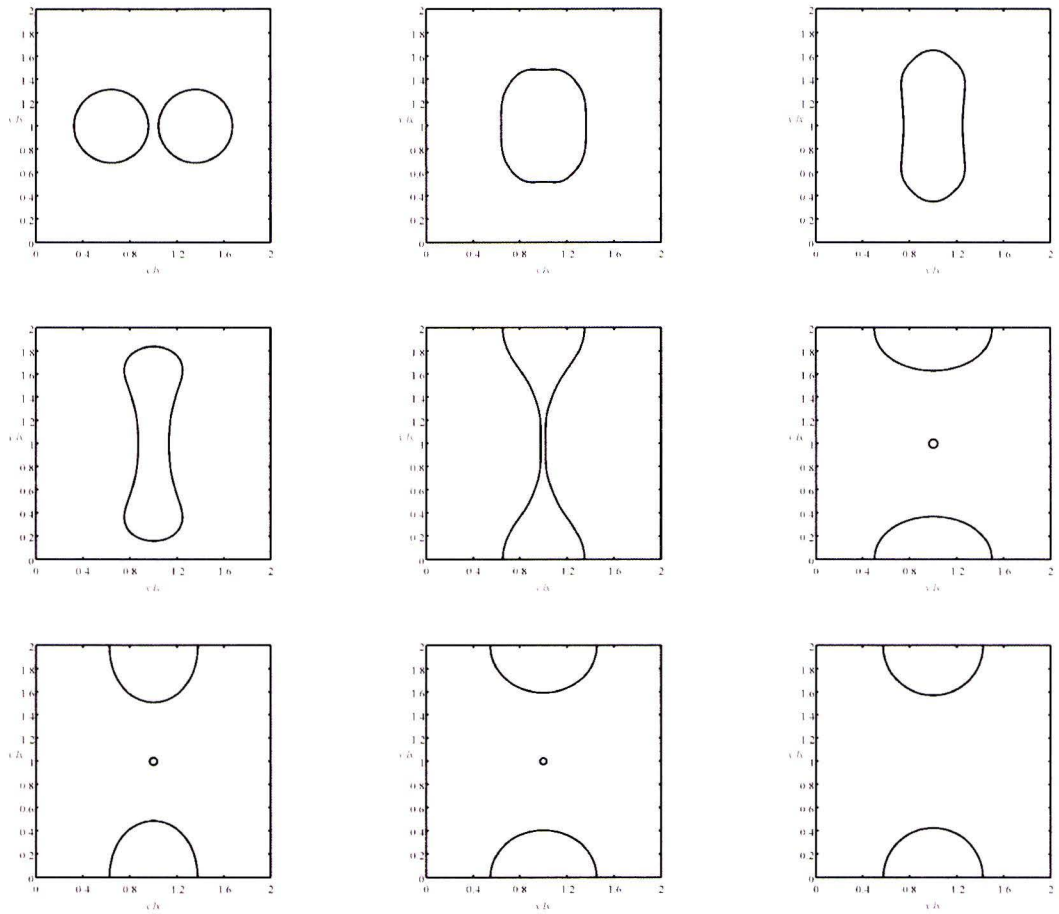


Figure 3.13: Two-dimensional drop collision simulation with  $Pr = 1$  and  $We = 42.8$  (Case Ne). From left to right and top to bottom: time evolution of the simulation at arbitrary subsequent times. The isoline of mass density is shown at the average.

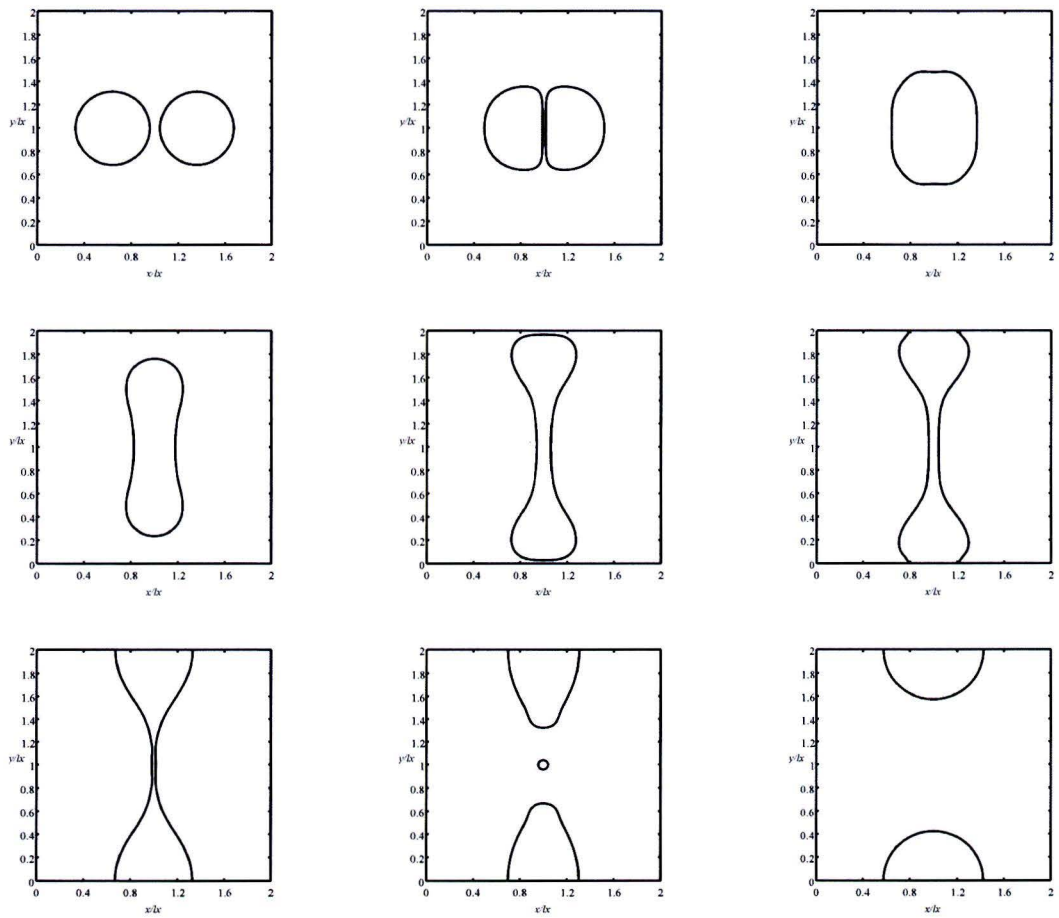


Figure 3.14: Two-dimensional drop collision simulation with  $Pr = 1$  and  $We = 119$  (Case Nf). From left to right and top to bottom: time evolution of the simulation at arbitrary subsequent times. The isoline of mass density is shown at the average.



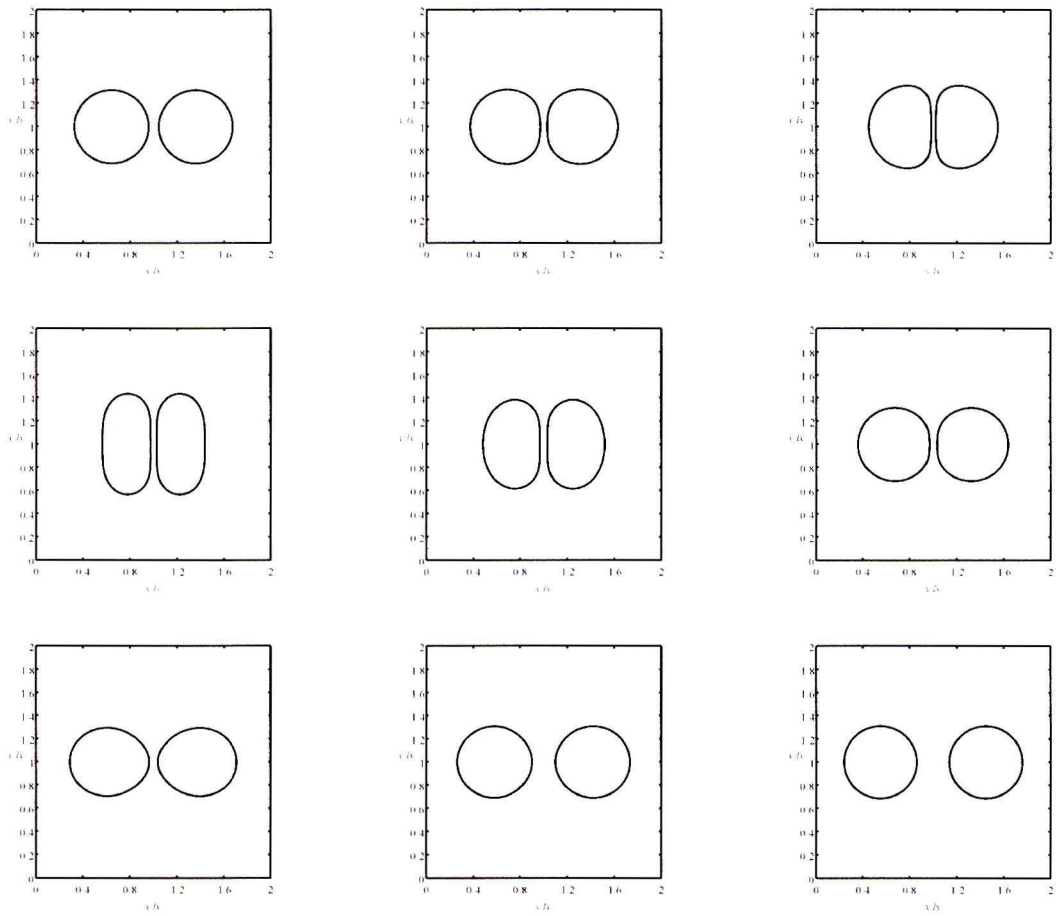


Figure 3.15: Two-dimensional drop collision simulation with  $Pr = 150$  and  $We = 10.7$  (Case Kj). From left to right and top to bottom: time evolution of the simulation at arbitrary subsequent times. The isoline of mass density is shown at the average.

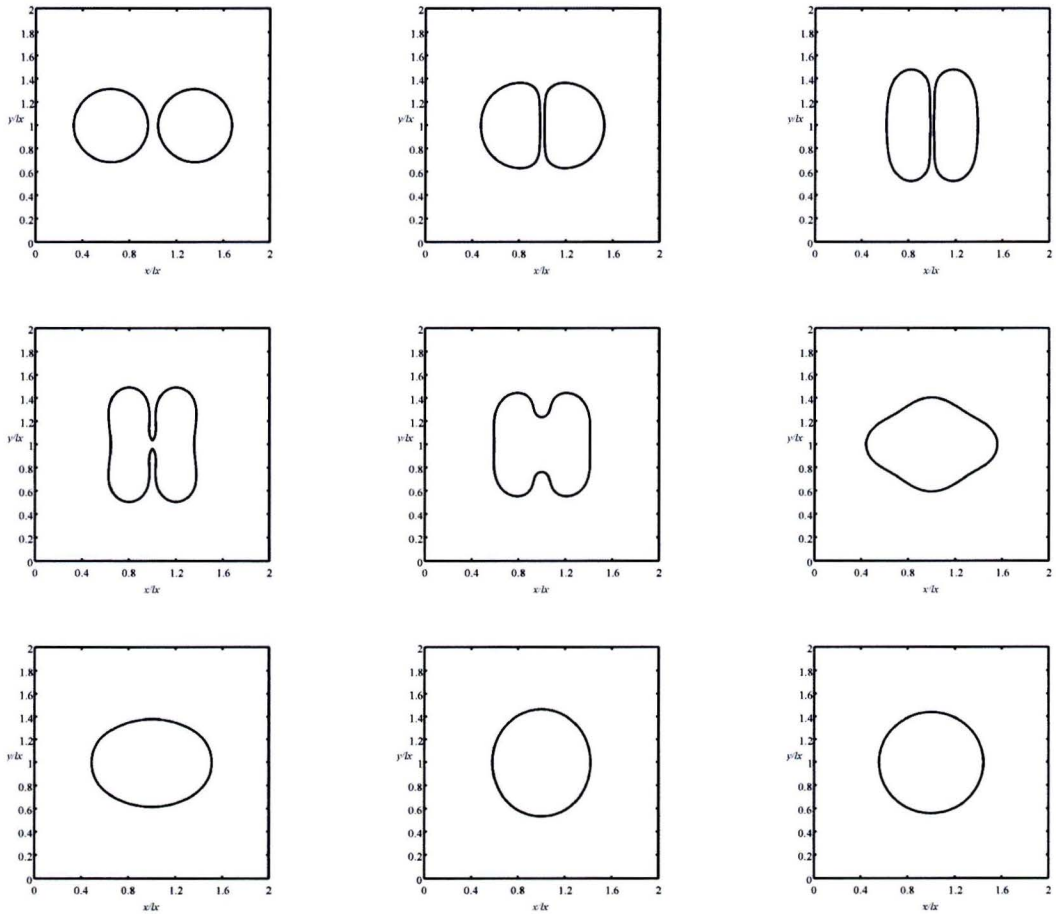


Figure 3.16: Two-dimensional drop collision simulation with  $Pr = 150$  and  $We = 19.0$  (Case Kk). From left to right and top to bottom: time evolution of the simulation at arbitrary subsequent times. The isoline of mass density is shown at the average.

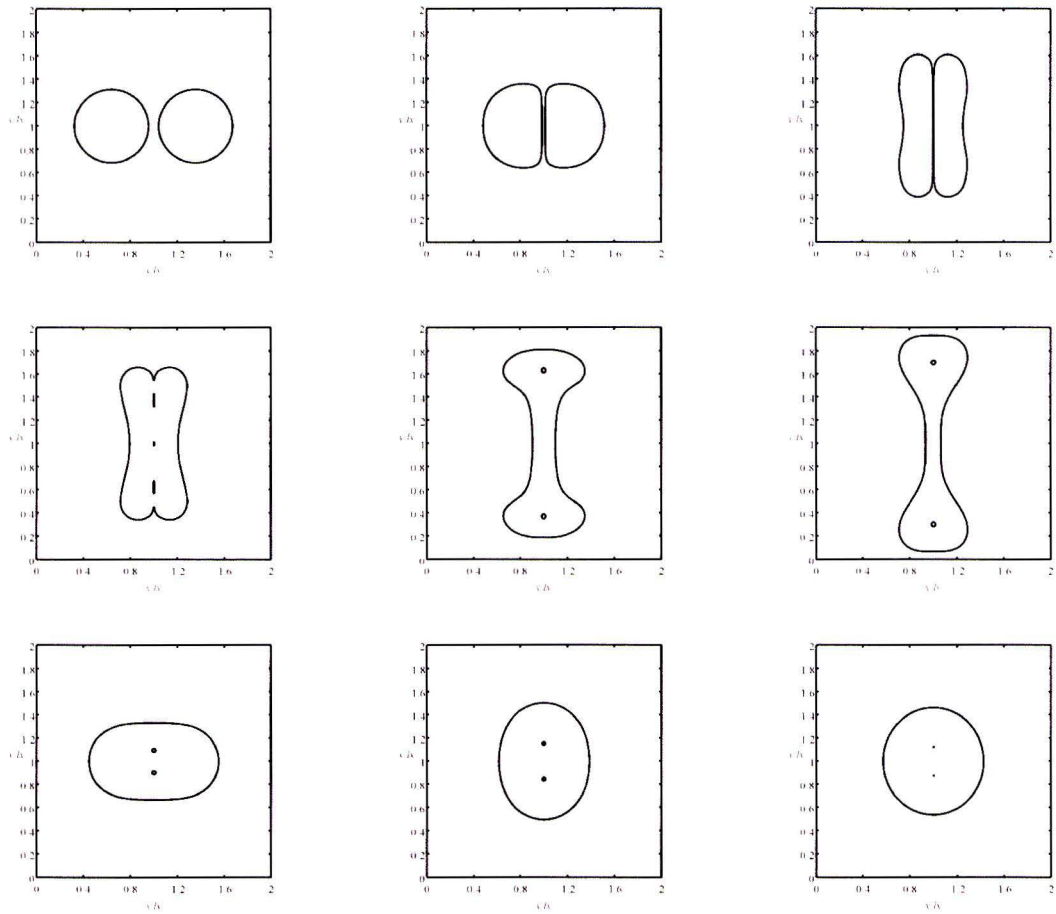


Figure 3.17: Two-dimensional drop collision simulation with  $Pr = 150$  and  $We = 119$  (Case Km). From left to right and top to bottom: time evolution of the simulation at arbitrary subsequent times. The isoline of mass density is shown at the average.

## Chapter 4

# Conclusions

The steam that is injected in the cross-flow condenses close to the injector as found by Clerx [6]. The momentum that the steam has induces a single phase jet. This jet is observed in the velocity fields [6] but also in the Temperature fields that were measured. The observed jet compares well to literature on single phase jets in cross flow. The coordinates of the center line for the jet temperature can be scaled with  $rd$ , with  $r$  the square root of the momentum ratio and  $d$  the diameter of the injector. The scaled trajectories compare well to the ones found in literature. The temperature decays along the jet trajectory as expected. The temperature measurements are however not accurate enough to make a good comparison with the decay of the temperature that is found in literature.

In some temperature-difference fields, beside the jet that is present for all temperature fields, a plume of high  $\Delta T$  is found. In contrast with the jet, this plume has no significant accompanying velocity component. This means that it originates purely from heat transferred to the cross-flow without momentum transferred to it. The plume is observed to occur for high cross-flow temperatures like 65 °C and 75 °C. For low steam mass flux (500 g/h) a plume is visible at cross-flow temperature of 25 °C but this plume is much smaller than the one observed for the higher cross flow. The jet trajectory is not changed much by the cross-flow temperature but the magnitude of the temperature difference with the cross-flow,  $\Delta T$ , is much lower for the higher cross flow temperatures. This shows that less heat is transferred to the jet as this energy is now used to create the plume. Clerx [6] observed that the penetration depth of steam in the cross-flow is dependent also on the cross-flow temperature and the steam mass flux with the latter one less important. A direct relation between the penetration depth of the steam and the amount of energy that is stored in the plume is therefore suspected.

The determination of the trajectories of the temperature center line is still rather inaccurate. For future measurements it is advisable to make sure that the sensors can be read out more accurately to avoid the error that the lack of accuracy may introduce. If a better accuracy is needed, the number of points where the temperature is measured may be increased. Also it is advisable to place the tips out of the wake of other sensors for future measurements. Although the position in the wake that one of the sensors occupies seems not to influence the flow around it, it would be better to avoid this situation for future measurements. It would be even better to implement non invasive methods like the laser induced fluorescence that has been investigated by Liew [13] or possibly shadowgraphy. This would have two advantages. First, a noninvasive measurement method doesn't influence the flow. Second, such a method would make it possible to measure the entire flow field including the region near the injector

which is actually the most interesting region.

The numerical method that is developed works well for one and two dimensional simulations. The use of the method is limited to small scales and temperatures close to the critical point. The behavior of the one dimensional phase separation simulation is much slower than a similar simulation for a model without the energy equation that is developed by Pecenko [15]. A linear stability analysis corresponds well to the results of the one dimensional phase separation analysis. From the stability analysis it follows that the reason for the slow behavior is the presence of heat effects corresponding with phase change. The model with the energy equation is therefore a better model for multi-phase flows, even for flows that are initially isothermal. Not implementing the energy equation leads to ignoring the energy that corresponds with phase change and will yield unphysical behavior.

The two dimensional drop retraction simulations show an oscillating droplet as expected. For refined grid sizes the solution converges to a unique solution. The surface tension that can be calculated based on the simulations corresponds well to an analytical value based on the used model for surface tension. This shows that the two dimensional simulations perform well. The energy equation that is present in the model makes it possible to simulate the evaporation of a saturated drop in a superheated vapor. The drop shrinks and disappears eventually. During the process the temperature inside the drop remains constant as would be expected for a saturated drop. The drop collision cases show some variations in the observed behavior. For a Prantl-number 1, the drops coalesce easily. For high collision speed, the drops break up after coalescence. For a Prantl-number 150, the drop collision looks entirely different. The drops deform severely before they coalesce. For low collision speeds drops have been observed to bounce back instead of coalesce. Because of the large deformation of the drops before coalescence, small bubbles have been observed to be entrapped by the drops. These effects are caused by local effects near the surface. For the higher Prantl-number, the heat conductivity is lower. The phase change that is necessary for the surface to coalesce occurs much more slowly.

The developed numerical method can be used to predict small scale two phase phenomena close to the critical point of the fluid. To increase the scale for which the method can be used, local grid refinement is an option. Iteratively changing the grid would however be cumbersome. A method like the volume of fluid method would be more suitable for the length scales that are characteristic for industrial applications. The diffuse interface method here developed can be used to predict surface conditions for such a method.

# Bibliography

- [1] D. M. Anderson, G. B. McFadden, A. A. Wheeler, Diffuse-interface methods in fluid mechanics, *Annu. Rev. Fluid Mech.* textbf30, 139 (1998).
- [2] D. M. Anderson, G. B. McFadden, A Diffuse-interface Description of fluid Systems, *NIST Int. Rep. 5887. Gaithersburg* (1996).
- [3] N. Ashgriz, J.Y. Poo, Coalescence and separation in binary collisions of liquid drops, *J. Fluid Mech.*, **221** 183 (1990).
- [4] J.W. Cahn, Free energy of a nonuniform system.II. Thermodynamic basis, *J. Chem. Phys.* **30**, 1121 (1995).
- [5] Y.A. Çenglel, M. A. Boles, Thermodynamics, An engineering approach, fourth edition, *McGraw-Hill* (2002).
- [6] N. Clerx, Experimental study of direct contact of steam in turbulent duct flow, *PhD-Thesis, Eindhoven University of Technology* (In progress).
- [7] B. Cockburn, H. Gau, a Model numerical scheme for the propagation of phase transitions in solids, *SIAM J. Sci. Comput.*, **17 5** 1092 (1996).
- [8] M.T. Heath, Scientific Computing: an introductory survey, second edition, *McGraw-Hill* (2002).
- [9] Y. Kamotani, I. Greber, Experiments on a Turbulent Jet in a Cross Flow, *AIAA Journal*, **10 11** 1425 (1972).
- [10] Y. Kamotani, I. Greber, Experiments on confined turbulent jets in cross flow, *NASA CR-2392*, (1974).
- [11] P.K. Kundu, I.M. Cohen, Fluid mechanics, fourth edition, *Academic press* (2008).
- [12] D.R. Lide, CRC Handbook of Chemistry and Physics, 84th edition 2003-2004, *CRC Press* (2004).
- [13] R. Liew, Phosphor Thermometry and Simulation of Direct Steam Injection, *master-Thesis, Eindhoven University of Technology* (2009).
- [14] B.D. Pratte, W.D. Baines, Profiles of the round turbulent jet in a cross flow, *J. Hydr. Div.*, **92**, 53 (1967).

- [15] A. Pecenko, J.G.M. Kuerten, C.W.M. van der Geld, A diffuse-interface approach to two-phase isothermal flow of a Van der Waals fluid near the critical point, *Int. j. multiphase flow*(2010).
- [16] S.H. Sith, M.G. Mungal, Mixing, structure and scaling of the jet in crossflow, *J. Fluid Mech.* **357**, 83 (1998).
- [17] C.W. Shu, S. Osher, Efficient implementation of essentially non-oscillatory shock-capturing schemes, *J. comp. phys.*, **77**, 439 (1988).

## Appendix A

# Influence of the temperature sensors on the mean flow

It is important to know the influence of the inserted temperature sensors on the flow field. In the ideal case, the flow field is not changed at all by the sensors. This will of course not happen because close to the sensors the temperature and flow field is distorted. The severity of the distortion is investigated here by performing PIV measurements on the flow with the sensors inserted. The velocity will be compared to the velocity that is observed for an undisturbed flow. To keep the experiments simple, there is no steam injection. There is only a flow of water through the square measurement section. This leads to a standard turbulent flow. As the flow is developed at the entrance of the measurement section, the profile does not change as a function of the coordinate in the flow direction.

A YAG-laser with a wavelength of 532 nm is used to illuminate the particles in the flow. The laser bundle is guided towards the test setup with a series of mirrors. The bundle is then stretched to a sheet by a set of three lenses. First a convex lens is used to focus the bundle in the middle of the test setup. A vertical-concave and a vertical-convex lens are used to stretch the bundle in the vertical direction. The three lenses together yield a thin vertical light sheet that cuts through the center of the measurement section.

To avoid the reflections from the laser light to be recorded, fluorescent particles are used as will be described in Clerx [6]. The particles emit light that has a different wavelength than the laser light. The camera is mounted with a notch filter that blocks the wavelength of the laser. In this way, only the fluorescent particles are recorded, not the reflections of the laser light.

The settings for the experiments without disturbances are shown in table A.1. This experiment is carried out and described by Nicole Clerx. The settings for the PIV and the evaluation can be found in [6]. The assumption of a developed flow is used to calculate the velocity profile. This is defined for the undisturbed experiment as the average over all PIV images but also averaged over all points in the flow direction (vertical). This yields the undisturbed profile that is compared with the disturbed flow.



Temperature (TI-104) [° C]	24.1
Pressure (PIC-103) [bar (absolute)]	5.58
Volume flow (FIC-106) [m <sup>3</sup> /h]	0.96
Reynolds number	$1.0 \cdot 10^4$

Table A.1: Experimental settings for the PIV measurements of the undisturbed flow as measured by Clerx [6]

For the disturbed flow, similar settings are used as shown in table A.2. The pressure is noticeably lower. The Reynolds-number is however almost the same. Therefore it is assumed that this different setting for the pressure does not change the velocity profile. Additional to the flow settings, table A.2 contains the PIV settings. An interrogation window of 32 by 32 pixels is used. The pulse delay is chosen such that the displacement of a particle is approximately 8 pixels. This is enough to ensure an accurate prediction of the velocity. For the evaluation, *PIVview* is used. A multi grid algorithm is used to find the right velocities. The velocity field for the disturbed flow is calculated as the average over all PIV images. Now we can not average over all locations in the vertical direction as the flow is known to change due to the inserted sensors. A median filter is used to remove erroneous vectors. These are not taken into account for calculating the average.

Temperature (TI-104) [° C]	25.2
Pressure (PIC-103) [bar (absolute)]	2.89
Volume flow (FIC-106) [m <sup>3</sup> /h]	0.96
Reynolds number	$1.000 \cdot 10^2$
Camera resolution	1008 x 1018
pixels per mm x	26.1667
pixels per mm y	25.4474
pulse delay [s]	0.00075
Number of frames per experiment	1000

Table A.2: Experimental settings for the PIV measurements with the temperature sensors inserted in the flow

The results of the measurements are shown in figure A.1, A.2 and A.3. The sub-figure on the left indicates the locations of the sensor and the lines along which the velocity is plotted for the measurements that are performed on the flow with the sensors inserted. In the sub-figure on the right, the vertical velocities are plotted. The markers represent the undisturbed velocity profile as measured by Clerx [6]. The lines represent the velocity profiles for the disturbed case. The color of the lines in the right sub-figure corresponds to the color of the lines in the left sub-figure.

It can be seen that the velocity upstream of the sensors is not influenced by the presence of the sensors. At the locations of the sensors the flow is locally disturbed. The velocity is lower near the sensors. The flow recovers fast, for example, in figure A.2 the upper profile shows no sign of the disturbance in velocity that was introduced in the velocity profile just below. Nevertheless, a disturbance downstream is clearly present. In figure A.3 for the second line from the top, the disturbance in the mean velocity upstream of the sensors is observed to be 20% of the value for the undisturbed flow.

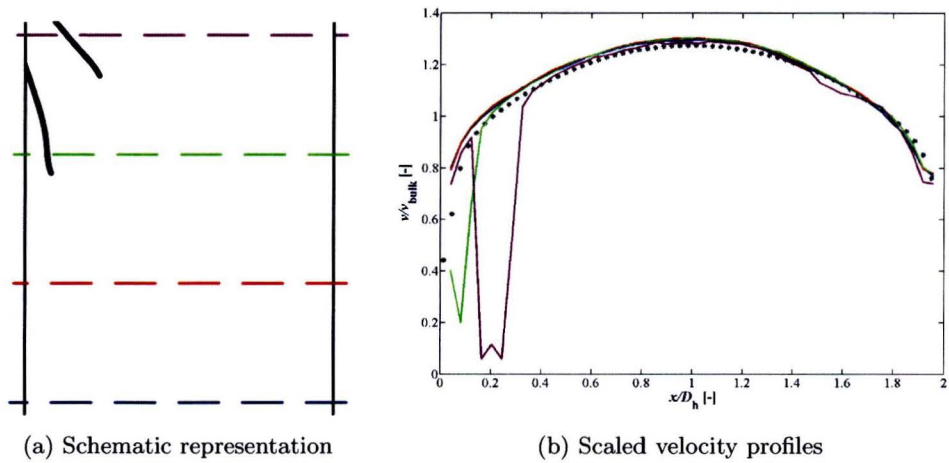


Figure A.1: Vertical velocity profiles for the setup with the inserted temperature sensors at the left of the channel

As the flow upstream is not influenced, we can conclude that the first two sensors (TI-128 and TI-126) measure the temperature as would be obtained from the undisturbed flow because the tips of these sensors are not in the wake of another one. The upper sensor (TI-127) is in the wake of the other two sensors as can be seen in the figures. The results of this sensor are reported in the main text but results of this sensor should be looked at with caution.

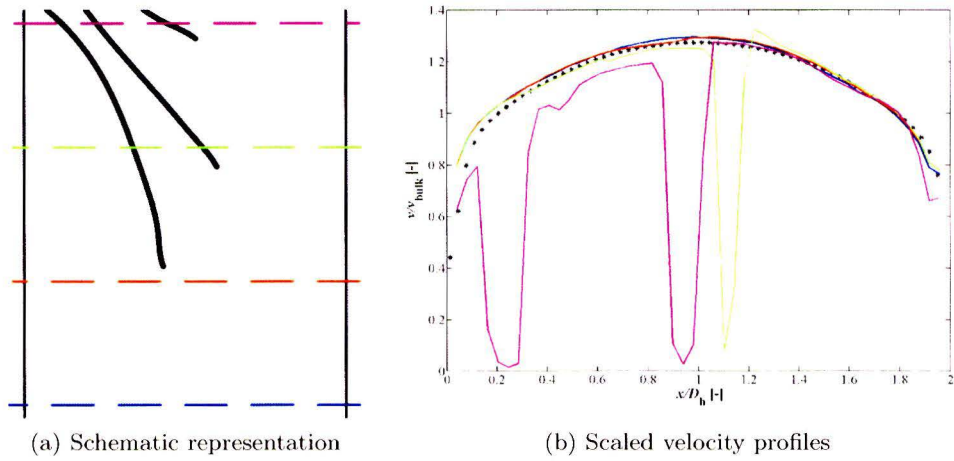


Figure A.2: Velocity profiles for the setup with the inserted temperature sensors in the middle of the channel

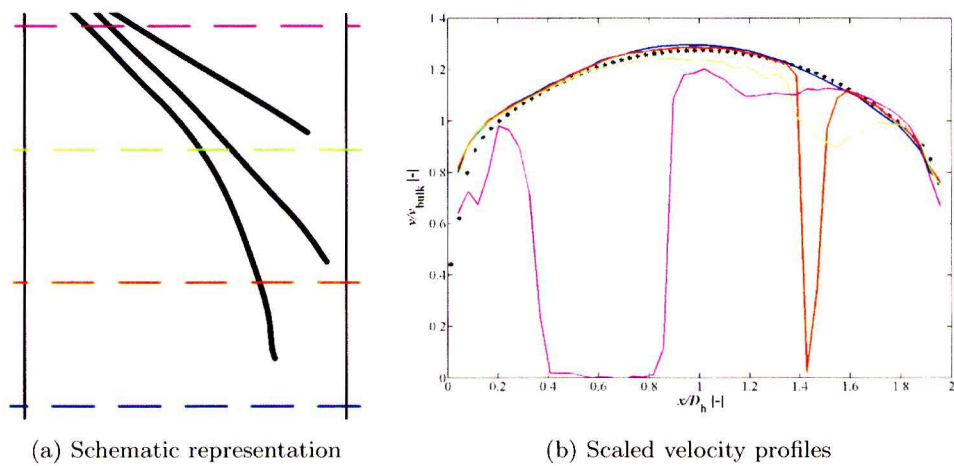


Figure A.3: Vertical velocity profiles for the setup with the inserted temperature sensors at the right of the channel

## Appendix B

# Calibration of Pt-100 temperature sensors

The temperature sensors that were used for the measurements that are used for generation of the temperature profiles are calibrated in a bath with a thermostat. The bath is filled with water. The temperature can be varied between room temperature and close below the boiling point of water. The Pt-100 temperature sensors are placed in the water close to a mercury-in-glass thermometer. The precision of the thermometer is 0.1 K. The precision of the Pt-100 sensors is also 0.1 K. The thermometer is used as the reference value for the temperature.

For the calibration of the sensors, the temperature measured by the Pt-100 sensors is compared to the value from the mercury in glass thermometer. The results are shown in table B.1. The Pt-100 sensors are indicated by their systematic names: TI-126, TI-127, TI-128 and TI-104.

Thermostat	Thermometer	TI-126	TI-127	TI-128	Thermostat	Thermometer	TI-104
26	26.6	31.2	31.1	31.1	26	26.2	26.2
30	30.8	35.3	35.3	35.3	30	30.6	30.5
35	35.6	40.3	40.2	40.3	35	35.5	35.5
40	40.7	45.3	45.3	45.3	40	40.1	40.0
45	45.7	50.5	50.4	50.5	45	45.0	45.0
50	50.6	55.4	55.3	55.3	50	50.4	50.5
55	55.5	60.4	60.3	60.3	55	54.9	55.1
60	60.4	65.3	65.3	65.3	60	60.2	60.5
65	65.5	70.6	70.5	70.5	65	65.0	65.3
70	70.4	75.5	75.4	75.5	70	69.9	70.3
75	75.2	80.5	80.4	80.5	75	74.9	75.5
80	80.0	85.5	85.3	85.5	80	79.8	80.4

Table B.1: Calibration measurements for the temperature sensors. Temperatures are given in  $^{\circ}C$

The results of the calibration are used to obtain a linear transformation from the temperature that is measured by the sensors to the temperature measured by the thermometer.

This Transformation has the form:

$$T_{Thermometer} = a * T_{Pt-100} + b \quad (B.1)$$

The constants  $a$  and  $b$  are determined by a least squares analysis on the data from table B.1. The values of  $a$  and  $b$  for the different sensors are shown in table B.2. If the fit is compared to the measurements from the thermometer, there will of course not be an exact fit. The standard error that is present in the fit is indicated in table B.2 by  $s$ . The standard error has the same order of magnitude as the accuracy of the thermometer and the sensors. This means that the linear fit is a good way of transforming the temperature of the sensors to the reference value that is measured with the mercury-in-glass thermometer. The latter value is in the report presented as the real temperature and its value can be determined with an uncertainty of 0.1 K by all sensors.

	TI-126	TI-127	TI-128	TI-104
m	0.983978308	0.985521344	0.983575663	0.986786768
b	-3.971008889	-3.978352507	-3.914876363	0.5073133
s	0.093146955	0.057608767	0.103039539	0.084526964

Table B.2: values of the fit parameters according to a least squares analysis of the data from table B.1

## Appendix C

# Experiments and settings for temperature measurements on steam injection

The measurements for the temperature field are described here. Every temperature field is built from the measurements of the temperature at ten different locations of the temperature sensors. Each measurement is carried out for two minutes and the temperature at the corresponding location is determined as the average over this period. The ten measurements together are called a set of measurements. These sets usually take half an hour to record. This includes the time that is needed to change the position of the temperature sensors. During this set of measurements, the settings for the flow rates of the cross flow and the steam, the pressure and the temperature of the cross-flow and the steam are kept constant. Table C.1, C.2 and C.3 show the sets of measurements and their settings. The values that are presented here are the average values over the time of the set.

The name of the cases is used to keep track of the different cases. During the set of measurements, the value of the variables can change a little bit. The temperature of the cross-flow,  $T_{cf}$ , is usually kept within  $0.5^\circ$  C of the set point. Because the temperature difference between the cross-flow and the probes is used, this does not introduce an error in the temperature fields.  $Q_{cf}$  is the volume flow of the cross-flow.  $P_{cf}$  represents the pressure in the cross flow.  $\dot{m}_v$  is the mass flow of the steam. The temperature of the steam is denoted by  $T_v$ . The deviation from the mean value is small for these settings. During a set of measurements the relative error amounts not more than four percent. The momentum ratio,  $J$ , is determined based on the mass flow of the steam and the volume flow of the cross flow. The densities as can be expected, based on the temperatures and pressures of the steam and the cross-flow, are used for this calculation.

name	25_a	25_b	25_c	25_d	25_e	25_f
date	19-10-09	16-11-09	16-11-09	16-11-09	19-10-09	16-11-09
$Q_{cf}$ [m <sup>3</sup> /h]	0.95	1.88	2.79	0.48	0.95	1.41
$P_{cf}$ [bar]	3.0	3.0	3.0	3.0	3.0	3.0
$T_{cf}$ [° C]	25	25	25	25	25	25
$\dot{m}_v$ [g/h]	492	996	1498	492	997	1499
$T_v$ [° C] 135	136	137	135	136	137	135
$J$ [-]	14.23	14.55	14.59	56.77	56.92	56.82

name	25_g	25_h	25_i	25_j	25_k
date	16-11-09	16-11-09	19-10-09	19-10-09	19-10-09
$Q_{cf}$ [m <sup>3</sup> /h]	0.32	0.63	0.95	0.95	0.95
$P_{cf}$ (absolute) [bar]	3.0	3.0	3.0	3.0	3.0
$T_{cf}$ [° C]	25	25	25	25	25
$\dot{m}_v$ [g/h]	492	997	1496	2000	3000
$T_v$ [° C]	135	136	137	136	136
$J$ [-]	126.81	129.44	124.86	-	-

Table C.1: Settings for the measurement sets at 25 ° C

name	65_a	65_b	65_c	65_d	65_e	65_f
date	20-10-09	18-11-09	18-11-09	18-11-09	20-10-09	18-11-09
$Q_{cf}$ [m <sup>3</sup> /h]	0.96	1.89	2.79	0.49	0.95	1.41
$P_{cf}$ [bar]	3.0	3.0	3.0	3.0	3.0	3.0
$T_{cf}$ [° C]	65	65	65	65	65	65
$\dot{m}_v$ [g/h]	496	998	1498	494	999	1497
$T_v$ [° C] 132	136	137	136	135	136	137
$J$ [-]	14.76	14.55	14.53	54.07	58.64	57.01

name	65_g	65_h	65_i	65_j	65_k
date	18-11-09	18-11-09	20-10-09	20-10-09	20-10-09
$Q_{cf}$ [m <sup>3</sup> /h]	0.33	0.64	0.95	0.96	0.96
$P_{cf}$ (absolute) [bar]	3.0	3.0	3.0	3.0	3.0
$T_{cf}$ [° C]	65	65	65	65	65
$\dot{m}_v$ [g/h]	494	994	1499	2000	3000
$T_v$ [° C]	135	136	137	136	136
$J$ [-]	122.36	124.65	125.73	-	-

Table C.2: Settings for the measurement sets at 65 ° C

name	75_a	75_b	75_c	75_d	75_e	75_f	75i
date	13-01-10	13-01-10	13-01-10	13-01-10	13-01-10	13-01-10	13-01-10
$Q_{cf}$ [m <sup>3</sup> /h]	0.95	1.90	2.79	0.49	0.96	1.48	0.96
$P_{cf}$ [bar]	3.0	3.0	3.0	3.0	3.0	3.0	3.0
$T_{cf}$ [° C]	75	75	75	75	75	75	75
$\dot{m}_v$ [g/h]	491	998	1499	494	999	1499	1500
$T_v$ [° C]	133	136	137	135	136	137	137
$J$ [-]	14.24	14.58	14.76	55.69	56.69	52.23	124.11

Table C.3: Settings for the measurement sets at 75 ° C



## Appendix D

# Thin plate spline interpolation with Matlab

A thin-plate smoothing spline is a way to find a fit through data on a two dimensional domain. In contrast with many other methods, data points can be chosen randomly in the domain. Methods like linear or cubic interpolation require often that sample points lie on a Cartesian grid.

The function 'tpaps' in Matlab finds a thin-plate smoothing spline  $f$  for the given data points. The general expression for the smoothing spline can be written as:

$$f(\bar{x}) = \sum_{j=1}^n C_j \Psi(\bar{x} - \bar{c}_j) \quad (\text{D.1})$$

The smoothing spline is defined by its centers  $c_j$  and its coefficients  $C_j$ . This way of defining a spline with a sum of fixed functions with different centers is called the scattered translate form. The spline is built up from circular basis functions  $\Psi$  defined as:

$$\Psi(\bar{r}) = |\bar{r}|^2 \log|\bar{r}|^2 \quad (\text{D.2})$$

The centers  $c_j$  are chosen equal to the sampling points. The coefficients are determined by minimizing the expression:

$$p\mathbf{E}(f) + (1 - p)\mathbf{R}(f) \quad (\text{D.3})$$

$\mathbf{E}$  is a measure for the error between the smoothing spline and the values at the data points.  $\mathbf{R}$  is a measure for the smoothness and is used to smoothen the effect of noise on the data points. Expressions for  $E$  and  $R$  are:

$$\mathbf{E}(f) = \sum_{j=1}^n |y_j - f(\bar{x})|^2 \quad (\text{D.4})$$

$$\mathbf{R}(f) = \int \left( \left| \frac{\partial^2 f}{\partial x_1^2} \right|^2 + \left| \frac{\partial^2 f}{\partial x_1 \partial x_2} \right|^2 + \left| \frac{\partial^2 f}{\partial x_2^2} \right|^2 \right) \quad (\text{D.5})$$

The smoothness parameter  $p$  can be chosen between 0 and 1.  $p = 0$  corresponds to a least squares approximation by a linear polynomial while  $p = 1$  corresponds to a thin spline

interpolation of the data where the spline  $f$  goes exactly through all the data points. In the temperature fields there are under 30 data points. Smoothing the data is therefore of little use. For constructing the approximate temperature fields we use a thin spline interpolation ( $p = 1$ ).

It can be observed that the size of the domain has almost no influence on the spline that is calculated by the Matlab function 'tpaps'. A stretching of the domain in one direction distorts the behavior dramatically. The reason for this must be sought in the round basic function  $\Psi$ . Stretched shapes can't be modeled with the round functions  $\Psi$ . As no severely stretched shapes are present in the temperature-difference fields, the thin plate spline interpolation works very well.

# Appendix E

## Description of the simulations

In the main text the simulations performed are briefly described. A complete overview of the simulations that are performed and their settings is given here. The cases all have a unique label to be able to distinguish them. The different simulations are grouped by their type and goal. The one dimensional simulations and simulations for drop retraction, evaporation and collision are discussed in separate sections below.

### E.1 One dimensional simulations

The one dimensional simulations are performed to provide some insight in phase separation. The cases named *1D.Random* start from a mean density and temperature with a disturbance added to them. This disturbance has a chaotic form. The simulations labeled *1D.LST* start from the same mean mass density and temperature. The disturbances that are imposed on the mass density  $\rho$ , Temperature and velocity now have a sinusoidal shape to make the behavior predictable. The cases *1D.Random* have symmetrical boundary conditions at the first and the last nodes. The cases *1D.LST* in contrary have periodic boundary conditions as required for the stability analysis that is performed in section 3.4. The sinusoidal initial disturbance is chosen such that it fits exactly in the domain so the periodic boundary condition holds. One dimensional simulations are performed for the isothermal model and the non isothermal model. For the cases with the isothermal model the temperature is assumed to be constant and pressure is only dependent on the local density of the fluid. The isothermal cases are labeled by: *.I*.

The material properties are the same for all one dimensional case and their values are shown in table E.1. A superscript \* indicates that a parameter is not defined for the isothermal model. The simulation parameters are shown in table E.2. They differ per simulation.

$a$	$0.558 \text{ Pa m}^6/\text{mol}^2$	$c1$	$1.875 \cdot 10^{-5} \text{ m}^2/\text{s}$
$b$	$6.51 \cdot 10^{-5} \text{ m}^3/\text{mol}$	$c2^*$	$3, 31 \cdot 10^{-2} \text{ m}^4/\text{s}^3\text{K}$
$M$	$0.03 \text{ kg/mol}$	$\rho_0^*$	$203.2 \text{ kg/m}^3$
$K$	$6.0 \cdot 10^{-11} \text{ Nm}^2/\text{kg}^2$	$e_0^*$	$0 \text{ J/kg}$
$C_v^*$	$1489.7 \text{ J/kg K}$	$T_0^*$	$305 \text{ K}$

Table E.1: Material constants for one dimensional simulations

Case label	<i>1D.Random.I</i>	<i>1D.Random</i>	<i>1D.LST.I</i>	<i>1D.LST</i>
number of grid points	800	800	800	800
iteration time step [s]	$2.45 \cdot 10^{-11}$	$2.45 \cdot 10^{-11}$	$2.45 \cdot 10^{-11}$	$2.45 \cdot 10^{-11}$
number of iterations	320001	8000001	80001	8000001
Writing interval	400	100000	100	10000

Table E.2: Simulation parameters for one dimensional simulations

The length of the domain is  $lx = 1.0 \cdot 10^{-4}$  m. The density  $\rho_0$  is 120 kg/m<sup>3</sup> and the temperature  $T_0$  is 290 K. The velocity is 0 m/s. A small disturbance is added to these values. For the cases *1D.Random*, there is only a disturbance added to the density.

$$\rho(x) = \rho_0 + \cos(7.5\pi x/x_l) + 2 \cos(\pi x/x_l) + 5e^{-20(x-0.25x_0)^2/x_0^2} \quad (\text{E.1})$$

here  $x_l$  is the length of the domain and  $x_0$  is the middle of the domain.

For the *1D.LST* cases the disturbance is much smaller because for our linear stability analysis, the disturbances must be very small. For the density, velocity and temperature, the following values have been implemented.

$$\rho = \rho_0 + \epsilon \cos(kx) \quad (\text{E.2})$$

$$u = \rho_0 \frac{-9.48 \cdot 10^4 \epsilon}{k\rho_0} \sin(kx) \quad (\text{E.3})$$

$$T = T_0 + 2.517 \cdot 10^{-2} \epsilon \cos(kx) \quad (\text{E.4})$$

Here  $\epsilon$  is a small value that is characteristic for disturbance.  $k$  is the wave number. The value of  $\epsilon$  is  $1 \cdot 10^{-4}$  and the wave number is set to  $k = 10\pi/x_l$  so there are 5 complete oscillations in the domain. The initial conditions for the *1D.LST* cases are defined in this way to closely match the unstable Eigen-mode that could be expected from theory.

## E.2 Drop retraction simulations

The drop retraction cases are labeled starting with a capital letter M. The simulations are performed on a two dimensional domain with symmetry boundary conditions at all walls. Due to these boundary conditions only a quarter of the drop is simulated. A schematic representation of the numerical initial condition is shown in figure E.1. The drop is initially longer in the x direction than the y direction.

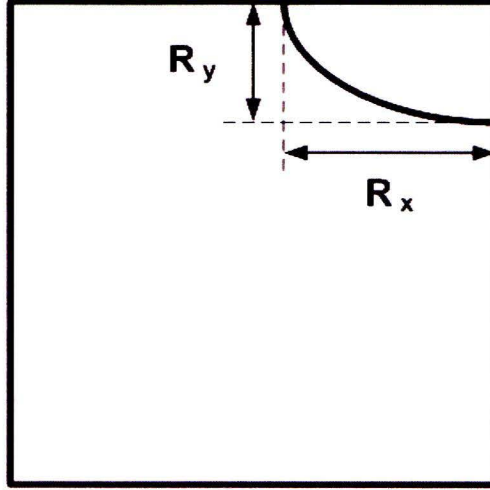


Figure E.1: Schematic representation of the numerical domain for the drop retraction simulations

All drop retraction cases that are performed for this report have the same material properties and initial conditions. The used material properties is shown in table E.3. The symbolic notation of the properties are chosen similar to the notation that is used in section 3.2. The initial conditions are shown in table E.4. The temperature is homogeneous as can be seen. For the specified densities, the initial pressure for vapor and liquid state is the same. The densities used here are the ones for saturated conditions. The saturated conditions are calculated as described in Appendix J.

$a$	$0.558 \text{ Pa m}^6/\text{mol}^2$	$c1$	$1.875 \cdot 10^{-5} \text{ m}^2/\text{s}$
$b$	$6.51 \cdot 10^{-5} \text{ m}^3/\text{mol}$	$c2$	$3,31 \cdot 10^{-2} \text{ m}^4/\text{s}^3 \text{ K}$
$M$	$0.03 \text{ kg/mol}$	$\rho_0$	$203.2 \text{ kg/m}^3$
$K$	$6.0 \cdot 10^{-11} \text{ Nm}^2/\text{kg}^2$	$e_0$	$0 \text{ J/kg}$
$C_v$	$1489.7 \text{ J/kg K}$	$T_0$	$305 \text{ K}$

Table E.3: Material constants for drop retraction simulations

Domain size $lx^2$	$(1.0 \cdot 10^{-4})^2 \text{ m}^2$
$\rho_{vapor}$	$86.09 \text{ kg/m}^3$
$\rho_{liquid}$	$223.49 \text{ kg/m}^3$
$T_{vapor}$	$290 \text{ K}$
$T_{liquid}$	$290 \text{ K}$
Initial length $R_x$	$3.87 \cdot 10^{-5} \text{ m}$
Initial length $R_y$	$2.74 \cdot 10^{-5} \text{ m}$
$\delta$	$2.0 \cdot 10^{-10} \text{ m}$

Table E.4: Initial conditions for drop retraction simulations

The number of grid points for the simulations is varied to assess whether the method converges to a unique solution for finer grids. The courant number, defined as

$$C_r = \frac{V * \Delta t}{\Delta l} \quad (\text{E.5})$$

is taken the same for all drop retraction simulations.  $V$  is the value of the velocity in a cell,  $\Delta t$  is the time step used in the simulation and  $\Delta l$  is here the distance between grid points.

The time step is therefore taken smaller for a higher number of grid points. The settings per case are shown in table E.5. The writing interval is the number of iterations at which results are written to file. The Case  $\text{Mb}_{extended}$  is just an extension of case Mb where the simulation is continued for more iterations.

Case label	Ma	Mb	Mc	$\text{Mb}_{extended}$
number of grid points	$200^2$	$400^2$	$800^2$	$400^2$
iteration time step [s]	$2.45 \cdot 10^{-10}$	$1.23 \cdot 10^{-10}$	$6.14 \cdot 10^{-11}$	$1.23 \cdot 10^{-10}$
number of iterations	600001	1200001	6000001	60000001
Writing interval	2500	5000	10000	100000

Table E.5: Simulation parameters for drop retraction simulations

### E.3 Drop evaporation

There is one drop evaporation case labeled H. Like before, symmetry boundary conditions are used on all four walls of the two dimensional domain. Again, only a quarter of the drop is simulated. A schematic representation of the numerical initial condition is shown in figure E.2. The initial condition is a circular drop that has a higher temperature than the surrounding vapor.

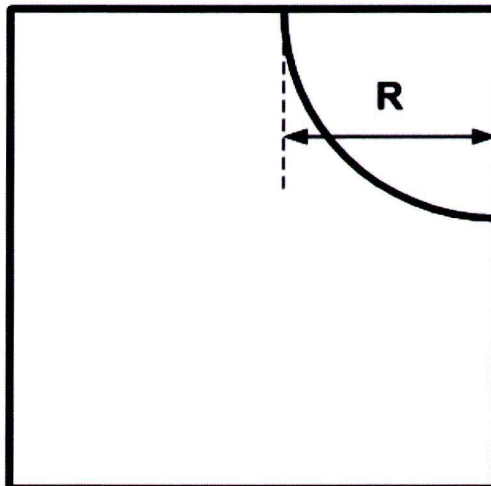


Figure E.2: Schematic representation of the numerical domain for the drop evaporation simulation

Material properties for the evaporation case are shown in table E.6. The initial conditions are shown in table E.8 The vapor on the outside is 50 Kelvin higher than the liquid drop. The densities are chosen such that the pressure of the vapor is the same as that of the liquid drop. The liquid is under saturated conditions as for the drop retraction case. The vapor is superheated. The simulation settings are shown in table E.7.

$a$	$0.558 \text{ Pa m}^6/\text{mol}^2$	$c1$	$1.875 \cdot 10^{-5} \text{ m}^2/\text{s}$
$b$	$6.51 \cdot 10^{-5} \text{ m}^3/\text{mol}$	$c2$	$3,31 \cdot 10^{-2} \text{ m}^4/\text{s}^3\text{K}$
$M$	$0.03 \text{ kg/mol}$	$\rho_0$	$203.2 \text{ kg/m}^3$
$K$	$6.0 \cdot 10^{-11} \text{ Nm}^2/\text{kg}^2$	$e_0$	$0 \text{ J/kg}$
$C_v$	$1489.7 \text{ J/kg K}$	$T_0$	$305 \text{ K}$

Table E.6: Material constants for drop evaporation simulation

number of grid points	$400^2$
iteration time step [s]	$1.23 \cdot 10^{-10}$
number of iterations	3600001
Writing interval	4000

Table E.7: Simulation parameters for drop evaporation simulation

Domain size $lx^2$	$(1.0 \cdot 10^{-4})^2 \text{ m}^2$
$\rho_{vapor}$	$53.37 \text{ kg/m}^3$
$\rho_{liquid}$	$223.49 \text{ kg/m}^3$
$T_{vapor}$	$340 \text{ K}$
$T_{liquid}$	$290 \text{ K}$
Initial radius R	$3.87 \cdot 10^{-5} \text{ m}$
$\delta$	$2.0 \cdot 10^{-10} \text{ m}$

Table E.8: Initial conditions for drop evaporation simulation

## E.4 Drop collision

The drop collision simulations consist of two drops of the same size that move to one another with the same speed. As before, symmetry boundary conditions are used on all four sides of the two dimensional domain. Due to symmetry, only half a drop has to be simulated to capture the total drop collision. The initial condition is shown schematically in figure E.3. The velocity in the vapor phase is zero while inside the liquid drop, the velocity has a uniform value.

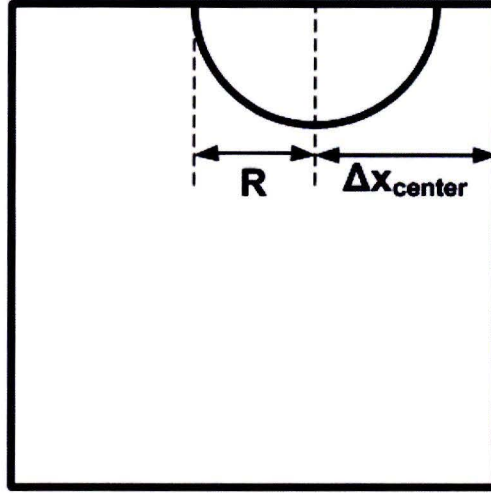


Figure E.3: Schematic representation of the numerical domain for the drop collision simulations

For the collision cases, the influence of the Prandtl-number on the simulation is investigated. There were two types of material used. The cases for which the Prandtl-number is 150, are labeled starting with an K. The material properties of these cases are shown in table E.9. The cases for which the Prandtl-number is 1, are labeled starting with an N. The material properties for these cases are shown in table E.10. As can be seen the difference between the K and the N series is the heat conductivity. This property is chosen 150 times higher for the cases with  $Pr = 1$ .

$a$	$0.558 \text{ Pa m}^6/\text{mol}^2$	$c1$	$1.875 \cdot 10^{-5} \text{ m}^2/\text{s}$
$b$	$6.51 \cdot 10^{-5} \text{ m}^3/\text{mol}$	$c2$	$2,21 \cdot 10^{-4} \text{ m}^4/\text{s}^3\text{K}$
$M$	$0.03 \text{ kg/mol}$	$\rho_0$	$203.2 \text{ kg/m}^3$
$K$	$6.0 \cdot 10^{-11} \text{ Nm}^2/\text{kg}^2$	$e_0$	$0 \text{ J/kg}$
$C_v$	$1489.7 \text{ J/kg K}$	$T_0$	$305 \text{ K}$

Table E.9: Material constants for drop Collision simulation, K series ( $Pr = 150$ )

$a$	$0.558 \text{ Pa m}^6/\text{mol}^2$	$c1$	$1.875 \cdot 10^{-5} \text{ m}^2/\text{s}$
$b$	$6.51 \cdot 10^{-5} \text{ m}^3/\text{mol}$	$c2$	$3,31 \cdot 10^{-2} \text{ m}^4/\text{s}^3\text{K}$
$M$	$0.03 \text{ kg/mol}$	$\rho_0$	$203.2 \text{ kg/m}^3$
$K$	$6.0 \cdot 10^{-11} \text{ Nm}^2/\text{kg}^2$	$e_0$	$0 \text{ J/kg}$
$C_v$	$1489.7 \text{ J/kg K}$	$T_0$	$305 \text{ K}$

Table E.10: Material constants for drop Collision simulation, N series ( $Pr = 1$ )

The simulations settings are shown in table E.11. There is a small difference between the settings for the cases from the K and the N series. The latter one is continued for a larger number of iterations.



number of grid points	400 <sup>2</sup>	number of grid points	400 <sup>2</sup>
iteration time step [s]	$1.23 \cdot 10^{-10}$	iteration time step [s]	$1.23 \cdot 10^{-10}$
number of iterations	800001	number of iterations	1600001
Writing interval	4000	Writing interval	8000

(a) K series

(b) N series

Table E.11: Simulation parameters for drop collision simulations

The initial conditions for all drop collision cases are quite similar. Like for the drop retraction simulations, the temperature in both the liquid and vapor phase is the same and the densities are chosen such that the fluid is saturated in both phases. The density under saturated conditions is calculated as described in appendix J. The distance between drops and the radius of the drops is not varied. Different initial velocities were prescribed for the different cases. Table E.12 summarizes the initial condition for all collision simulations.

Domain size $lx^2$	$(1.0 \cdot 10^{-4})^2 \text{ m}^2$	Kh	2.5 m/s	Na	2.5 m/s
$\rho_{vapor}$	86.09 kg/m <sup>3</sup>	Ki	5.0 m/s	Nb	5.0 m/s
$\rho_{liquid}$	223.49 kg/m <sup>3</sup>	Kj	7.5 m/s	Nc	7.5 m/s
$T_{vapor}$	290 K	Kk	10 m/s	Nd	10 m/s
$T_{liquid}$	290 K	Kl	15 m/s	Ne	15 m/s
Initial radius $R$	$3.16 \cdot 10^{-5} \text{ m}$	Km	25 m/s	Nf	25 m/s
$\Delta x_{center}$	$4.4 \cdot 10^{-5} \text{ m}$				
$\delta$	$2.0 \cdot 10^{-10} \text{ m}$				

(a)

(b) Initial velocities

Table E.12: Initial conditions for drop collision simulations

## Appendix F

# Two-dimensional model for the governing equations

The equations given in section 3.2 are the general equations. For the two-dimensional simulations that are performed, a two-dimensional form can be written that can be used in the simulations. In this section, deviates with respect to time or space are denoted by subscripts t, x and y. u and v represent the velocity components in x and y direction respectively.

Conservation of mass yields in two dimensions:

$$\rho_t + (\rho u)_x + (\rho v)_y = 0 \quad (\text{F.1})$$

The x-momentum equation can be written as:

$$\begin{aligned} (\rho u)_t + (\rho uu)_x + (\rho uv)_y = & -[p(\rho, T)]_x + \left[ \frac{4}{3} \mu(\rho) u_x \right]_x - \left[ \frac{2}{3} \mu(\rho) v_y \right]_x - [\mu(\rho)(v_y + u_x)]_y \\ & + \left\{ [K \left[ \left( \rho \rho_{xx} - \frac{1}{2} (\rho_x)^2 \right) + \left( \rho \rho_{yy} - \frac{1}{2} (\rho_y)^2 \right) \right]] \right\}_x - [K \rho_x \rho_y]_y \end{aligned} \quad (\text{F.2})$$

for the y-momentum equation:

$$\begin{aligned} (\rho v)_t + (\rho vv)_y + (\rho uv)_x = & -[p(\rho, T)]_y + \left[ \frac{4}{3} \mu(\rho) v_y \right]_y - \left[ \frac{2}{3} \mu(\rho) u_x \right]_y - [\mu(\rho)(u_y + v_x)]_x \\ & + \left\{ [K \left[ \left( \rho \rho_{xx} - \frac{1}{2} (\rho_x)^2 \right) + \left( \rho \rho_{yy} - \frac{1}{2} (\rho_y)^2 \right) \right]] \right\}_y - [K \rho_x \rho_y]_x \end{aligned} \quad (\text{F.3})$$

The energy equation is written:

$$(E)_t + (uE)_x + (vE)_y = (kT_x)_x + (kT_y)_y - (K\rho(u_x + v_y)\rho_x)_x - (K\rho(u_x + v_y)\rho_y)_y + \nabla \cdot (\mathbf{u} \cdot (\mathbf{d} + \mathbf{T})) \quad (\text{F.4})$$

Here E represents the total energy:

$$E = \rho(e + \frac{1}{2}(u^2 + v^2)) + \frac{1}{2}K(\rho_x^2 + \rho_y^2) \quad (\text{F.5})$$

The work done by the forces can be written in components:

$$\nabla \cdot (\mathbf{u} \cdot (\mathbf{d} + \mathbf{T})) = \left( \mu \left( \frac{4}{3} uu_x - \frac{2}{3} uv_y + vv_x + vu_y \right) \right)_x$$

$$\begin{aligned}
& +(\mu(\frac{4}{3}vv_y - \frac{2}{3}vu_x + uv_x + uu_y))_y \\
& +((-p + K\rho(\rho_{xx} + \rho_{yy}) + \frac{1}{2}K(\rho_x^2 + \rho_y^2))u - (K\rho_x^2u + K\rho_x\rho_yv))_x \\
& +((-p + K\rho(\rho_{xx} + \rho_{yy}) + \frac{1}{2}K(\rho_x^2 + \rho_y^2))v - (K\rho_y^2v + K\rho_x\rho_yu))_y \tag{F.6}
\end{aligned}$$

The program uses the above equations to simulate the behavior. For every step in the finite volume method, The new density  $\rho$ , x-momentum  $\rho u$ , y-momentum  $\rho v$  energy  $E$  are calculated by using the discretized form of the equations F.1, F.2, F.3 and F.4. The values of the temperature and pressure from the previous time step are used. The new values of pressure is now calculated using the Van der Waals equation 3.12. The new temperature is calculated using equations F.5 and 3.17.

## Appendix G

# Derivation of conservative form of the energy equation

The equations that describe the diffuse interface method are found by Anderson [1]. For application of the finite volume method it is easier to work with the conservative form of the equations. The mass and momentum equations were already written in conservative form by Pecenko [15]. It is necessary to write the energy equation [1] also in conservative form. The steps taken are described here. First we recite the Gauss theorem for an arbitrary scalar, vector or tensor  $Q$ : from Kundu [11](equation 2.30).

$$\int_A Q \cdot \mathbf{n} dA = \int_V \nabla \cdot Q dV \quad (\text{G.1})$$

For a fixed material volume and an arbitrary function  $F(\mathbf{x}, t)$  [11](equation 4.5):

$$\frac{D}{Dt} \int_V F(\mathbf{x}, t) dV = \int_V \frac{\partial F}{\partial t} dV + \int_A F \mathbf{u} \cdot \mathbf{n} dA \quad (\text{G.2})$$

This can be rewritten:

$$\frac{D}{Dt} \int_V F(\mathbf{x}, t) dV = \int_V \frac{\partial F}{\partial t} dV + \int_V \nabla \cdot (F \mathbf{u}) dV \quad (\text{G.3})$$

Anderson [1] gives the following equation for the energy.

$$\frac{D}{Dt} \int_V \rho(\rho E) dV = \int_A (\mathbf{u} \cdot (\mathbf{d} + \mathbf{T})) \cdot \mathbf{n} dA - \int_A (\mathbf{q} + \mathbf{j}_E) \cdot \mathbf{n} dA \quad (\text{G.4})$$

Applying Gauss theorem and formula for the time derivative of a material volume, the equation can be rewritten.

$$\int_V \frac{d}{dt} (\rho E) + \nabla \cdot (\rho E \mathbf{u}) dV = \int_V \nabla \cdot (\mathbf{u} \cdot (\mathbf{d} + \mathbf{T})) dV - \int_V \nabla \cdot (\mathbf{q} + \mathbf{j}_E) dV \quad (\text{G.5})$$

The integration can be omitted to obtain the weak form .

$$\frac{\partial(\rho E)}{\partial t} + \nabla \cdot (\rho E \mathbf{u}) = \nabla \cdot (\mathbf{u} \cdot (\mathbf{d} + \mathbf{T})) - \nabla \cdot \mathbf{q} - \nabla \cdot \mathbf{j}_E \quad (\text{G.6})$$

This equation has a conservative form and is therefore used in our finite volume method.

## Appendix H

# Numerical validation of 1D stability analysis

The stability analysis that is described in section 3.4 can be compared with the results of a one dimensional simulation. A special simulation has been performed for this. The mean density, temperature and velocity are uniform in the domain. The density has been chosen in the unstable region of the phase diagram. A small disturbance is added to this. The disturbance has a sinusoidal form and fits exactly 5 times in the domain. The stability analysis requires a periodic boundary condition at the first and last point of the domain. A simulation for the isothermal model and one for the non-isothermal model are performed. The details of the simulations are described in appendix E.

In figure H.1, the evolution of the density profile is shown for some arbitrary times during the simulations. For both the isothermal and the non-isothermal model the initial disturbance grows till the stable saturated condition is reached. Both cases show in their final state 5 drops. The difference in the saturation densities that can be observed is caused by a temperature change in the non-isothermal simulation. The temperature rises approximately 3 K. This causes the difference between the vapor and liquid saturation density to be smaller.

To compare the simulations with the stability analysis in section 3.4, we compute an approximation for the imaginary part of  $\omega$  as used in the stability analysis. This approximation can be computed for every iteration step  $n$ :

$$\omega_a(t_n) = \ln \left( \frac{A(t_n)}{A(t_{n-1})\Delta t} \right) \quad (\text{H.1})$$

Here  $A(t_n)$  is the amplitude of the disturbance in the density as function of time. The amplitude is defined as the difference between the maximal density and the value of the mean density at the start of the simulation.  $t_n$  and  $t_{n-1}$  are the times at the sequential iterations.  $\Delta t$  is the difference between the two times.

The evolution of  $\omega_a$  is shown in figure H.2 for both the isothermal and the non-isothermal simulations. There appears to be some similarity between the two figures. For both cases  $\omega_a$  is constant for the first iterations. This shows that the initial amplitude is chosen small enough so the linear stability analysis is applicable for both cases. After some time the non-linear effects start playing a role. It can be seen that for both cases the nonlinearity increases the amplitude growth rate. When the densities reach their equilibrium values, the amplitude stops growing and  $\omega_a$  goes to zero. For the non-isothermal simulation, this is a

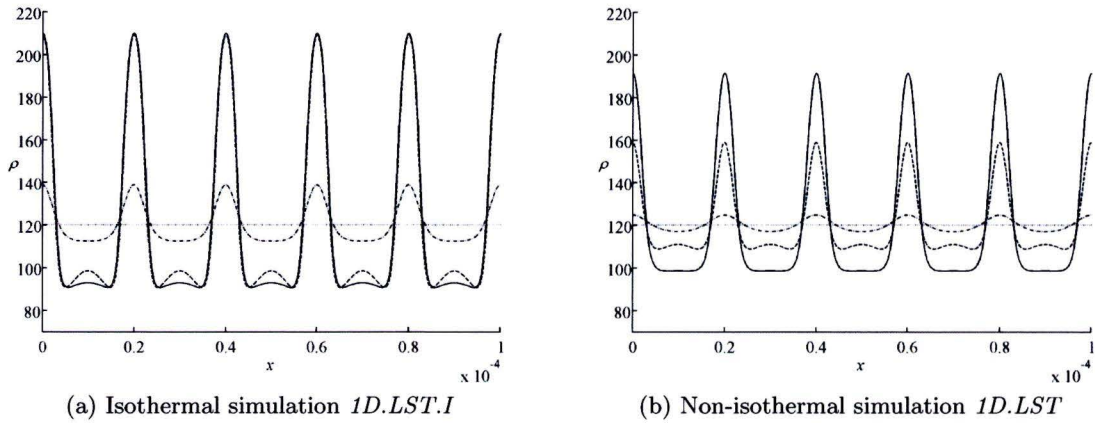


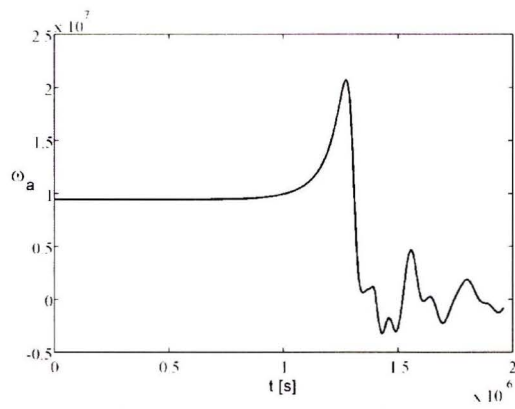
Figure H.1: Evolution of the density for the one dimensional linear stability analysis. Density is plotted for several time steps

	$\omega_a$ (simulation)	$Im(\omega)$ (analytical)
Isothermal	$9.41 \cdot 10^6$	$9.4197 \cdot 10^6$
Non-isothermal	$9.48 \cdot 10^4$	$9.4779 \cdot 10^4$

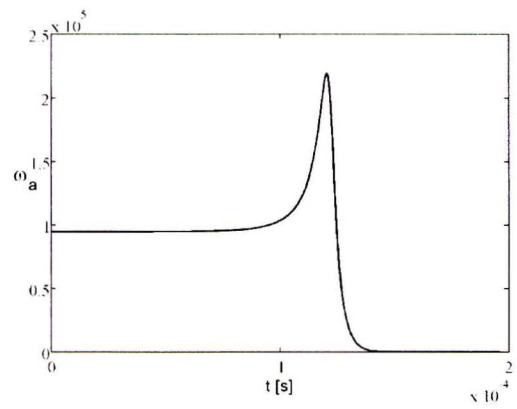
Table H.1: Comparison of the analytical and numerical values for the linear stability analysis

smooth process. The isothermal simulation shows some oscillation explaining the chaotic behavior of  $\omega_a$ . The most important difference that can be deduced is the difference between the value for  $\omega_a$ . For the non-isothermal simulations the value is approximately one hundred times smaller than for the isothermal one.

Comparing the values that are found for  $\omega_a$  at the first iterations to the analytical value for  $Im(\omega)$  as could be calculated for the case that is presented here leads to very good results. The values for the are presented in table H.1. This shows that the simulations perform very well.



(a) Isothermal simulation *1D.LST.I*



(b) Non-isothermal simulation *1D.LST'*

Figure H.2:  $\omega_a$  as function of time for the one dimensional simulations *1D.LST*

# Appendix I

## Programming

This Appendix is meant to give an overview of the used programming. The files itself are provided digitally. A short description of the files is given here.

### I.1 Experimental

During the experiments Labview was used for data logging. The data from various temperature sensors, pressure sensors and flow sensors is supplied in text files. The locations of the sensors are recorded with a camera that is mounted perpendicular to the plane of motion of the jet. The time span corresponding to each single measurement (note that it takes ten measurements to obtain the temperature fields) is recorded manually. To translate the obtained data to the temperature fields and other plots that are presented in the main text, several evaluation steps have to be performed. The files that have been used for this are described here.

#### **Image2Positions.m**

This file plots the images of the measurement section and lets you select the locations of the tips of the temperature sensors. The coordinates are stored in simple text files.

#### **master.m**

The data from the sensors is read in and the assembling of the time plots is directed. For the actual plotting the file *plot\_file.m* is called.

#### **plot\_file.m**

This file constructs the temperature fields with the Matlab function 'tpaps' as described in appendix D. The positions that are determined with the file *Image2Positions.m* are used as data points while the values are calculated for times that are supplied in the file *master.m*. The temperature difference of the sensors Ti-126, Ti-127 and Ti-128 with the sensor Ti-104 is plotted.

#### **Self\_similarity\*\*.m**

The Temperature fields that were made with the file *plot\_file.m* are plotted in one figure for a specific temperature. The plots are ordered by steam injection mass flow and momentum ratio.



### **line\_plot.m**

For a line through a temperature field, this file finds the local maximum along that line. It writes the coordinates and the value of this maximum to a file. Due to limited accuracy of the sensors, a difference of 0.1 K can not be distinguished. Therefore, an error-estimate for the coordinates is calculated as half the width along the line in which temperature stays within this 0.1 K from the local maximum. An estimate of the distance traveled along the jet axis is calculated for the predicted jet trajectory based on (2.2) with the parameters  $A$  and  $m$  determined by a fit through all data points from all fields. **lines.m**

This file defines three lines along which the local maximum is determined and writes the coordinates, value and the and an error estimate for the coordinates to a file for each temperature field. For the actual calculation, the file *line\_plot.m* is used.

### **scatterplot.m**

using the data that is obtained with the files *line\_plot.m* and *lines.m*, this script plots the trajectories of the temperature center lines. The Error bars are plotted in the graphs. The value at the centerline is also plotted.

### **Proces\_variables.m**

Calculates the mean values of the experimental settings like volume flow, mass flow and pressures. This provides a more accurate indication of the conditions that the simulations are performed in.

## **I.2 Numerical**

Here the scripts used for the diffuse interface method are described. First the diffuse interface method is described. The method is programmed in Fortran. second, the Matlab scrips that are used for evaluation are described.

### **Fortran programm**

The Diffuse interface method is implemented in a Fortran program. This program consist of several files that have each a different function. The Function of the files is explained below. The Fortran files for the drop retraction case Mb are added digitally. The files for the one dimensional simulations are different from the two dimensional simulation. But the components have the same function. Files for the one dimensional simulation are also provided digitally.

### **main.f**

This file calls the other files in the right order and writes the results of the simulation to output files at the specified times.

### **main.dat**

Contains values material and simulation properties.

### **storage.inc**

All global variables are defined. No values are assigned but types and sizes are defined.

#### **input.f**

Values are assigned to the material properties and simulation parameters.

#### **cond\_init.f**

Initial conditions for the density momentum and energy are prescribed.

#### **discretisation\_2D.f**

The fluxes that are used in the finite volume method as described in section 3.3 are calculated based on a discretized version of the two dimensional equations given in appendix F

#### **R\_K\_eva.f**

Using the flux that are calculated with discretisation\_2D.f. This file applies the TVD-Runge Kutta method that is described in section 3.3

#### **boundary\_par.f**

To calculate the spatial derivatives numerically near the boundary, a row of two grid points is specified outside the domain. The values at the grid points outside the domain is determined by the boundary conditions. This file updates the values of the simulation variables at these points after every step in the simulation.

#### **machine**

This file specifies the processors on which the simulation will be ran.

#### **makefile**

This file is used to translate the fortran for compilation and linking the fortran files and generating an executable program.

#### **Matlab scripts**

For the evaluation of the different cases a number of Matlab scripts is generated. Most of them are specific to a certain type of simulation. The most important files will be described here. They are also provided digitally.

#### **plotpar.m**

The plotpar.m file is used for every two dimensional simulation. The output of the simulations written to data files. Plotpar.m reads these files and plots density or temperature. The quarter domain that is used in the simulation is mirrored to get the full domain. Plotting velocities or energy is also possible with this script.

#### **Temperature.m & density.m**

These files are used for the drop retraction and the drop evaporation case to plot The density and Temperature in horizontal direction trough the center of the drop. Plots at several times are plotted in one figure to observe the evolution as function of time.

#### **furterInvestigation.m**

This is used for analyzing the drop retraction cases. Like the `plotpar.m` file, this script reads the data for the simulation output. The data is used to calculate the total mass and energy in the domain by summing over all data points. From this the relative errors in mass and energy conservation can be computed. The location of the interface is determined as the place where the density is equal to the mean of the density for the gas and the liquid. The evolution horizontal and the vertical radius is plotted against time. The surface tension is evaluated with formula 3.32. The radius is determined as described and the pressure at the drop center and the far field are used to calculate the pressure difference. The surface tension along the horizontal line and along a diagonal line is evaluated. A small difference is present because the drop is not exactly circular due to the rectangular grid.

### **figures1D.m**

For several times the density and temperature are plotted for the one dimensional simulations.

### **Analysis.m**

To compare the one dimensional results to the analytical solution for the linear stability analysis, the amplitude growth is monitored and plotted against time as discussed in appendix H

## Appendix J

# Saturation properties and surface tension

The calculation of saturation properties for the Van der Waals fluid is important for determining the initial conditions of the simulations. Two phases of the same fluid can only coexist in equilibrium if both phases have the same temperature and pressure. Additionally they should both be under saturated conditions. Surface tension is an important phenomenon for two phase mixtures. To verify that the simulations work correctly, the surface tension is calculated based on the Kortweg stresses in an analytical way.

### J.1 Saturation properties

For equilibrium, the temperatures of both phases should be the same to avoid heat transfer by conduction. Pressures should be the same to avoid pressure driven flow. The Gibbs free energy of the phases is the same, as shown by Çengel [5]. The Gibbs free energy is a thermodynamical potential that reaches a minimum for equilibrium states. For the specific Gibbs free energy, the following relation holds:

$$dg = -sdT + \nu dP \quad (\text{J.1})$$

The second term on the left is rewritten to obtain:

$$dg = -sdT + d(\nu P) - P d\nu \quad (\text{J.2})$$

In terms of the density this becomes:

$$dg = -sdT + d(P/\rho) + (P/\rho^2)d\rho \quad (\text{J.3})$$

This can be integrated as:

$$g = - \int s dT + P/\rho + \int (P/\rho^2) d\rho \quad (\text{J.4})$$

To obtain the equilibrium conditions, we have to solve the system:

$$P(\rho_v)/\rho_v + \int_0^{\rho_v} (P/\rho^2) d\rho = P(\rho_l)/\rho_l + \int_0^{\rho_l} (P/\rho^2) d\rho \quad (\text{J.5})$$

$$P(\rho_v) = P(\rho_l)$$

Here the subscripts  $l$  and  $v$  refer to the liquid and the vapor phase respectively. For our case, the pressure is calculated with the Van der Waals equation for the temperature of interest. Note that the term  $\int sdT$  is not present in the equation because the temperature of both phases is the same. The system is solved numerically with Maple to obtain the saturation densities for the temperature of interest. The calculated densities are used as initial conditions for the two dimensional simulations as described in appendix E

## J.2 Surface tension

The surface tension results from the gradient energy terms in the equations from section 3.2. Cahn [4] has derived an analytical equation for the surface tension for a system that has a Helmholtz free energy that is dependent, not only on the density but also on the gradient of the density. For a system with this gradient term equal to  $\kappa(\nabla\rho)^2$  and  $\kappa$  not dependent on  $\nabla\rho$  they find that surface tension can be defined by:

$$\sigma = \int [2\kappa(\nabla\rho)^2] d\mathbf{x} \quad (\text{J.6})$$

and

$$\kappa(\nabla\rho)^2 = \Delta F(\rho) \quad (\text{J.7})$$

The meaning of  $\Delta F$  will be explained below, but first we can rewrite :

$$1 = \sqrt{\frac{\kappa}{\Delta F(\rho)}} \nabla\rho \quad (\text{J.8})$$

multiplication with  $d\mathbf{x}$  on both sides leads to:

$$d\mathbf{x} = \sqrt{\frac{\kappa}{\Delta F(\rho)}} d\rho \quad (\text{J.9})$$

This is used to rewrite equation (J.6) to obtain an equation for the surface tension that is independent of the spatial variable  $\mathbf{x}$ :

$$\sigma = 2 \int_{\rho_1}^{\rho_2} [\kappa \Delta F(\rho)]^{1/2} d\rho \quad (\text{J.10})$$

In the above equations  $\Delta F$  is defined as:

$$\Delta F(\rho) = F(\rho) - F_0(\rho) \quad (\text{J.11})$$

$F$  is here the Helmholtz free energy per unit volume if the fluid would have a uniform density  $\rho$ .  $F_0$  is the Helmholtz free energy per unit volume with mean density  $\rho$  where both vapor and fluid phases would be present under equilibrium conditions. This means that  $F_0(\rho)$  can be calculated as an interpolation of  $F(\rho)$  between the saturation densities  $\rho_l$  and  $\rho_v$  calculated before. In Çengel [5], it can be found that for the specific Helmholtz free energy the following relation holds:

$$f = -sdT - Pdv \quad (\text{J.12})$$

As temperature is uniform at equilibrium, the free energy compared to a reference state with zero density at the temperature of interest is defined as:

$$F(\rho) = \rho \int_0^\rho (P(\rho_i)/\rho_i^2) d\rho_i \quad (\text{J.13})$$

The Helmholtz free energy corresponding to the gradient terms in the model we use is  $\frac{1}{2}K_E(\nabla\rho)^2$ . This means that  $\kappa = \frac{1}{2}K_E$  and we can write (J.10) as:

$$\sigma = \sqrt{2} \int_{\rho_v}^{\rho_l} [K_E \Delta F(\rho)]^{1/2} d\rho \quad (\text{J.14})$$

The formulas (J.11), (J.13) and (J.14) are implemented in the Maple script that was already used for the calculation of the saturation densities.